

DEVELOPMENT OF A HIGH SPEED THREE-DIMENSIONAL  
FLOW VISUALIZATION TECHNIQUE

Except where reference is made to the work of others, the work described in this thesis is my own or was done in collaboration with my advisory committee. This thesis does not include proprietary or classified information.

---

Aman Satija

Certificate of Approval:

---

Anwar Ahmed  
Associate Professor  
Aerospace Engineering

---

Brian Thurow, Chair  
Assistant Professor  
Aerospace Engineering

---

Roy Hartfield  
Professor  
Aerospace Engineering

---

George T. Flowers  
Interim Dean  
Graduate School

DEVELOPMENT OF A HIGH SPEED THREE-DIMENSIONAL  
FLOW VISUALIZATION TECHNIQUE

Aman Satija

A Thesis

Submitted to

the Graduate Faculty of

Auburn University

in Partial Fulfillment of the

Requirements for the

Degree of

Master of Science

Auburn, Alabama  
December 17, 2007

DEVELOPMENT OF A HIGH SPEED THREE-DIMENSIONAL  
FLOW VISUALIZATION TECHNIQUE

Aman Satija

Permission is granted to Auburn University to make copies of this thesis at its discretion, upon request of individuals or institutions and at their expense. The author reserves all publication rights.

---

Signature of Author

---

Date of Graduation

## VITA

Aman Satija, son of Madan Kumar Satija and Shashi Satija was born on 17<sup>th</sup> April 1980 at Agra in the state of Uttar Pradesh in India. He graduated from high school in 1997. He then pursued Mechanical Engineering from the Army Institute of Technology starting July 1998 and graduated 1<sup>st</sup> class in July 2002. He then worked for Voltas Pvt Ltd between July 2002 and Jan 2003. He worked for Kanbay Software Pvt Ltd in their credit card service division between Jan 2003 to Dec 2004 followed by a stint with Electronic Data Systems (EDS) for 6 months until June 2005. He entered Graduate School at Auburn University's Department of Aerospace Engineering in August 2005.

THESIS ABSTRACT

DEVELOPMENT OF A HIGH-SPEED THREE-DIMENSIONAL  
FLOW VISUALIZATION TECHNIQUE

Aman Satija

Master of Science, December 17, 2007  
(B.E, Pune University, 2002)

96 Typed Pages

Directed by Brian Thurow

A high-speed three-dimensional flow visualization technique has been developed. The technique involves the generation of laser pulses at a high repetition rate, which are subsequently converted to sheets of light and incrementally scanned across the flow field. The interaction of the laser sheet with particles contained in the flow results in scattering of the laser beam. This scattering is then imaged with a high-speed camera and the images are transferred to a computer where they are post-processed to produce three-dimensional images and movies of the flow. The development of the technique is described in terms of the development and characterization of two of its chief components: a pulse burst laser system and a high-speed scanning mirror. The 3<sup>rd</sup> generation pulse burst laser is capable of generating pulses at a repetition rate between DC to 10MHz with pulse widths as short as 20ns. This flexibility in repetition rate and pulse width was achieved by the use of an Acousto-Optic Modulator (AOM) for pulse

slicing. The contrast ratio of the pulses was 20000:1. The pulses were subsequently amplified by double passing them through a chain of 3 amplifiers. The gain of the 1<sup>st</sup> and 2<sup>nd</sup> amplifier was observed to be 16 and 142 respectively versus an anticipated gain of 200. The pulses could be uniformly amplified within duration of 600 microseconds in the gain curve. Various laser scanning options are discussed. Out of the various options the galvanometric scanning mirror was found to be most suitable for the development of the current technique. The maximum angular velocity of the mirror was measured to be in excess of 100,000 degrees/second over a 150 microsecond period with the mirror capable of accessing over 18 resolvable spots every 1  $\mu$ sec. The mirror was found to be highly repeatable in its position at a given time past the electronic trigger. Also given the high deflection efficiency of the mirror (>98%), it proves to be the best option for high-speed laser scanning.

Low speed 3-D visualization experiments were conducted to test the effectiveness of various components of the high-speed system and gauge the potential of the laser scanning concept. The experiments were conducted using a 15mW He-Ne laser in place of the pulse burst laser system. A low-speed flow field was created using the natural convection of smoke where the flow velocity was less than 1m/s. A DRS Hadland Ultra 68 camera was used to capture sequence of 2-D images. The 2-D sequence of images obtained was reconstructed into a 3-D image using Matlab. The camera resolution was 220\*220 pixels with the overall volume of the imaging region being 3.8" x 3.8" x 3.1". The 3-D results revealed several interesting features of the flow field. These results clearly demonstrate exciting possibilities arising from 3-D flow visualization.

## ACKNOWLEDGEMENTS

I am grateful to Dr Brian Thurow for his invaluable guidance over the past 2 years spanning my Master's Graduate work. Through his mentorship I have not only learnt valuable technical skills but also on how to think about engineering and scientific issues. His accessibility and patience encouraged me to think independently and provided a conducive environment to experiment.

I am grateful to Bradley Diedrick and Zhiguo Xu for their assistance in setting up the experiments and for their valuable inputs on the control aspect of the processes. I thank my family for providing unconditional support towards my endeavors and for making all the sacrifices that made it possible for me to pursue my educational goals.

Style used: AIAA Journal

Software used: Microsoft Word, Matlab, Microsoft Excel

## TABLE OF CONTENTS

LIST OF FIGURES .....	x
1 INTRODUCTION.....	1
1.1 Background of experimental fluid dynamics .....	1
1.2 Overview of the thesis.....	3
1.3 Evolution of laser scanning techniques.....	5
1.4 Pulse burst laser systems in high-speed laser diagnostics.....	7
1.5 Space and time scales in a flow field .....	9
2 PULSE BURST LASER SYSTEM.....	13
2.1 Overview .....	13
2.2 Pulse Slicing Mechanism .....	17
2.2.1 AOM Concept.....	17
2.2.2 Pulse Slicing.....	23
2.2.3 Post AOM pulse characteristics .....	25
2.3 Laser Amplifier Chain.....	29
3 HIGH-SPEED SCANNING AND IMAGING SYSTEMS.....	40
3.1 Overview .....	40
3.2 Scanning system parameters .....	42
3.3 Various scanning systems .....	44
3.3.1 Acousto-Optic deflectors .....	44
3.3.2 Electro-Optic deflectors.....	49
3.3.3 Rotating/Galvanometric scanning mirrors.....	50
3.4 High-Speed imaging systems.....	55
4 LOW SPEED 3-D FLOW VISUALIZATION EXPERIMENTS.....	60
4.1 Motivation.....	60
4.2 Experimental setup.....	61
4.3 Experimental results.....	67
5 CONCLUDING REMARKS .....	78
REFERENCES .....	81

## LIST OF FIGURES

Figure 1.1	Schematic of laser sheet scanning method.....	4
Figure 1.2	Flow diagram of a generic pulse-burst laser system. ....	7
Figure 2.1	Schematic of a typical AO interaction. The sound wave propagates in the upward direction whereas the laser beam propagates obliquely towards the right.....	18
Figure 2.3	Schematic of the pulse slicing mechanism using acousto-optic modulator ....	1
Figure 2.4	Pulse shape for 10, 20, 30, 40 and 50 nsec duration pulses. ....	26
Figure 2.5	A burst of four 20 nsec pulses separated by 200 nsec each (5 MHz).....	28
Figure 2.6	Oscilloscope trace of a 100 pulse burst of pulses at 100 KHz. Each pulse is 20 nsec in duration. ....	28
Figure 2.7	Schematic of power amplifier chain for AU pulse burst laser system. ....	30
Figure 2.8	Photograph of the overall layout of the pulse burst laser system.....	31
Figure 2.9	Photograph of the amplifier chain with the main components labeled. The lines with arrows pointing in both directions indicated double pass of the beam before entering the glan prism.....	31
Figure 2.10	Oscilloscope trace of the gain profile of the 2 <sup>nd</sup> amplifier with time on the X axis and gain on the Y axis along with the electrical trigger signal. ....	35
Figure 2.11	Oscilloscope trace of the combined gain from the 1st and the 2nd amplifier on the Y axis with time on the X axis along with the electrical trigger signal. ....	37

Figure 2.12 Oscilloscope trace of a 20ns pulse shape pre and post amplification. The squiggle which is on the pre-amplified pulse is due to certain EM interference from another device. ....	38
Figure 3.1 Schematic of proposed volumetric flow measurement system. ....	41
Figure 3.2 Photograph of acousto-optic deflector experimental set-up.....	48
Figure 3.3 Schematic and photograph of experimental set-up of laser and scanning mirror. ....	52
Figure 3.4 Scan angle vs command input voltage. ....	52
Figure 3.5 Response (deflection angle) of mirror to a step input command.....	53
Figure 3.6a Polynomial curve fit to data shown in Fig. 3.....	53
Figure 3.6b Angular velocity vs. time for a step input command.....	53
Figure 4.1 Schematic of the experimental set-up of laser and scanning mirror. ....	61
Figure 4.2 Photograph showing the incense sticks, DRS Hadland camera and the direction of laser propagation. ....	62
Figure 4.3 Photograph showing the incense sticks which created the flow field fixed in thermocole.....	63
Figure 4.4 Labview block diagram for generating the staircase waveform.....	65
Figure 4.5 Labview block diagram for creating a trigger signal for triggering the camera. ....	65
Figure 4.6a Staircase waveform generated to control the mirror location.....	66
Figure 4.6b Enlarged view of the staircase waveform between 0 to 0.14V. The steps in the staircase are clearly visible. ....	66
Figure 4.6c The input parameters for the staircase waveform are given above .....	67

The numbers above indicate the input parameters for the trigger waveform ..... 67

Figure 4.7 - Photograph of a dot card used for image registration. .... 69

Figure 4.8 Twelve images (out of a 68 image sequence) of the scattering of light from rising smoke. Each frame constitutes a different 2-D slice through the flow field. .... 70

Figure 4.9a 3-D picture of smoke rising from four incense sticks. Image is taken within the laminar regime of the flow..... 72

Figure 4.9b Overhead view of Fig. 4.9a showing more detail about the 3-D structure of the smoke plumes..... 72

Figure 4.10 Twelve images (out of a 68 image sequence) of the scattering of light from rising smoke. Each frame constitutes a different 2-D slice through the flow field. .... 73

Figure 4.11a 3-D image of smoke subjected to a disturbance forcing transition. .... 74

Figure 4.11b Enlarged view of the flow structure towards the front in 4.10a. .... 74

Figure 4.12a Cross-Sectional view of the front facing flow structure in 4.11a ..... 75

Figure 4.12b Enlarged view of the counter rotating vortices in 4.11a..... 75

Figure 4.13a 3-D image of interacting smoke plumes as they transition to turbulent flow. .... 76

Figure 4.13b 3-D image of interacting smoke plumes in turbulent regime..... 76

# 1 INTRODUCTION

## 1.1 Background of experimental fluid dynamics

Fluids are involved in many practical applications and an understanding of how they behave in different flow regimes is vital to many applications. The study of fluid problems is inherently complicated due to the nonlinear nature of the governing Navier Stokes equations. Understanding of fluids is currently being advanced by computational fluid dynamics (CFD), analytical fluid dynamics and experimental fluid dynamics (EFD). CFD is increasingly being used to obtain numerical solutions for various flow regimes; however, due to limitations of computing capacity, it is difficult to obtain reasonable solutions to complex fluid problems especially at high Reynolds Numbers. Some examples of such flows are flows around high-speed projectiles such as a space shuttle or reacting flows such as within scramjets or other combustion devices. For such complex fluid problems and flows at high Reynolds numbers, experiments are necessary to obtain an understanding of physical mechanisms involved and validate the computational models being developed to solve these problems.

Traditionally, experimental techniques have been limited to intrusive instruments such as pitot tubes and hot-wire anemometers; however, the use of intrusive methods is limited in high temperature, high pressure and other severe flow environments. In addition, intrusive measurements can potentially alter the very flow in which the

measurements are to be made. The use of non-intrusive optical diagnostics becomes imperative to study such flows. Early forms of optical techniques include schlieren and shadowgraph; however, they offer only line of sight integrated measurements and are primarily qualitative in the information they provide. More recently, the development of the laser has led to new, more advanced methods for making flow measurements. Commonly, experimental data is obtained by imaging the scattering or the fluorescence radiation from a flow field on to an optical detector, such as a CCD camera. The digital image can then be post processed and correlated to a mathematical model to obtain the properties of the flow field.

Qualitative and quantitative flow imaging, for the better part of the last century, was limited to point and planar measurements. It was realized, however, that to understand the physical mechanisms underlying several types of flows, a 3-D picture of the flow field was necessary. Different techniques such as stereography [Guezennec et al 1994], holography [Royer et al 1997], tomography [Elkins et al 2003] and laser sheet scanning [Yip et al 1988, Patrie et al 1994 and other researchers] have been used to obtain 3-D flow images. Even though stereography, holography and tomography are capable of 3-D imaging, their implementation requires complex and sensitive optical set-ups. These techniques are also limited by lower camera resolution, restricted optical access in flow facilities and costs. The laser sheet scanning method has proved to be easier to implement and its concept is relatively straightforward however, in the past the application of laser scanning techniques were limited to low speed flows due to limitations in laser and camera technology.

## 1.2 Overview of the thesis

This thesis describes the development of a high-speed 3-D flow visualization system. Development of the system is ongoing and this thesis focuses on the overall system design and the characteristics of its main components that make high-speed 3-D flow imaging possible. A laser sheet scanning approach has been chosen as the basis for development of the system. In addition, results from a set of low speed 3-D flow visualization experiments are reported which provide insight into the 3-D scanning concept and performance of the scanning and imaging components.

Figure 1.1 is a schematic of a typical laser sheet scanning setup. The concept of laser sheet scanning involves incremental deflection of a burst of pulses across a flow field by means of an optical scanner. These pulses can be converted into a sheet resulting in deflection of 2-D laser sheets across a flow field. Appropriate seeding of the flow is used to scatter or fluoresce the radiation onto a camera. In this manner, a sequence of 2-D images can be obtained. These images can then be post processed to obtain a 3-D reconstruction of the flow field.

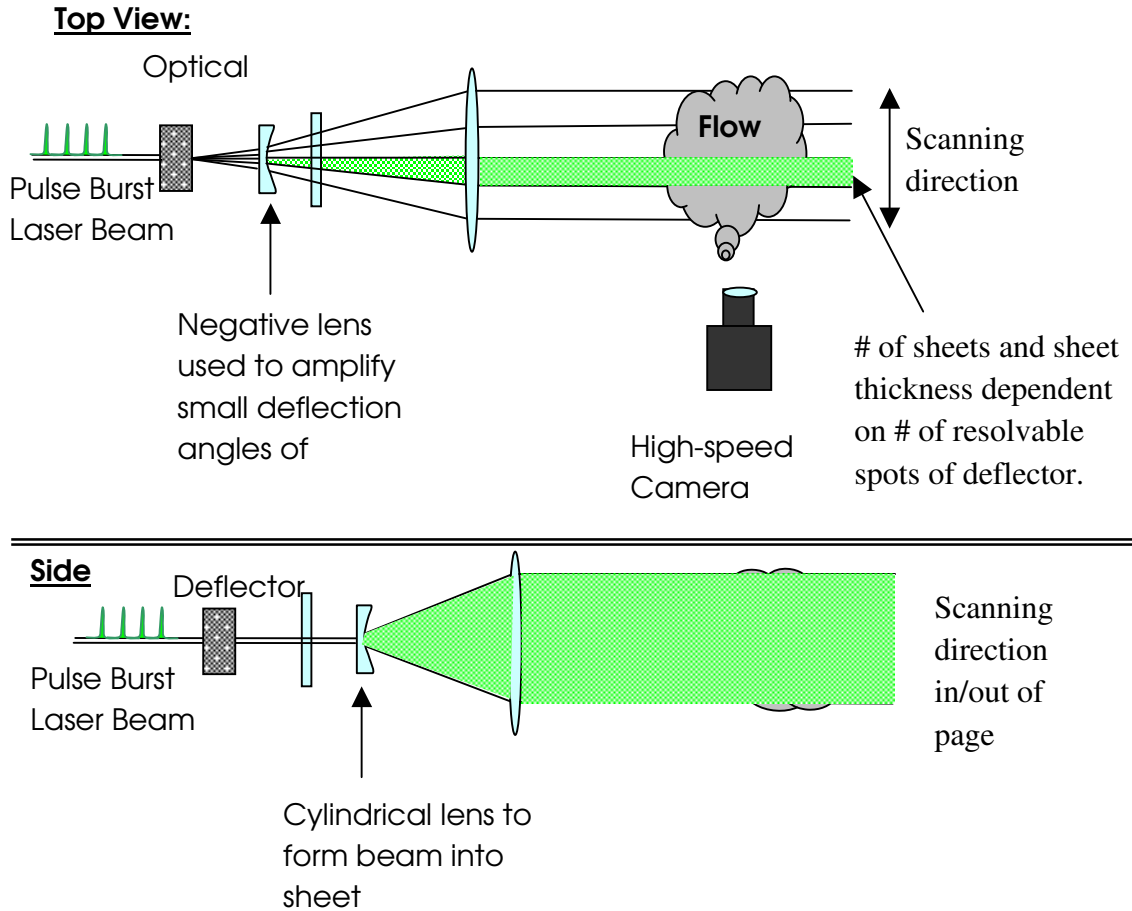


Figure 1.1 Schematic of laser sheet scanning method.

Recent advances in camera and laser technology have enabled the development of this high-speed flow visualization system. The development of a MHz high repetition rate laser source is crucial to the development of a high-speed 3-D flow visualization technique. Details of the laser development are presented in Chapter 2, which is exclusively dedicated to the laser design along with the characterization of the laser. It is written such that it can be read independently of the rest of the thesis. The scanning and imaging system must have the desired characteristics to match the high operational frequency achieved by the laser in order to perform high-speed flow imaging. The

scanning and imaging systems are described in Chapter 3, section 3.1 and 3.2 respectively. A series of low speed flow visualization experiments were conducted to gain experience with high-speed scanning and imaging equipment and to gain insight into the potential of 3-D flow visualization. These experiments are described in Chapter 4. This is followed by concluding remarks and comments on the potential for future development of the technique in Chapter 5.

### 1.3 Evolution of laser scanning techniques

Even though the field of laser scanning is relatively new, several efforts have been made in the last couple of decades to do laser sheet scanning to obtain 3-D flow images. The important imaging parameters while doing laser sheet scanning are the energy contained in each laser pulse, the speed of the sheet across the flow field, framing rate of the camera and the duration of exposure. Various types of lasers, scanning and imaging systems have been employed in the past to do 3-D imaging. An excellent review of the same can be found in a book titled “Flow Visualization: Techniques and Examples” by Smits and Lim [2000].

Early efforts at high-speed laser scanning were made by Long and Yip (1998). They used a resonant scanning mirror to deflect the output of a dye laser with a 1.4  $\mu\text{sec}$  long dye pulse (FWHM) from a Coumarin 440 dye laser across the flow field. During the sweep of this single pulse, 12 images, each with a resolution of 58 x 120 pixels, were acquired with an electronic framing camera operating at 10 MHz framing rate. This technique was improved upon by Patrie et al (1994) using a higher energy pulsed dye laser (10 J/pulse), a 12 sided polygonal mirror rotating at 30,000 rpm and a camera

capable of acquiring 20 images at a resolution on the order of 120 x 90 pixels for each image. A slower flow was imaged in 3-D by Kychakoff et al [1987]. They imaged a laminar premixed flat flame using an ArF excimer laser capable of producing 300mJ/pulse at 193nm at repetition rates up to 250 Hz. Island et al [1995] also used a dye laser which provided 3J at 590 nm for 2  $\mu$ sec. They used Mie scattering from condensed alcohol droplets to obtain 10 frames at  $10^7$  Hz. The scanning method differed as they used a 12-sided aluminum polygon rotating at 30,000 rpm. This effort may be considered the first instantaneous 3-D flow visualization of a supersonic flow. The use of dye lasers had the advantage of providing sufficient energy but they were inflexible in their operation. The fixed pulse duration of dye lasers makes it difficult to use cameras with different framing rates and the exposure duration in the case of using fixed pulse duration would be always determined by the camera repetition rate. Also since only a part of the laser energy would be used for imaging the rest of the pulse energy would be wasted.

Hult et al 2002 used a cluster of four double-pulses Nd:YAG lasers, a galvanometric scanning mirror and an 8-CCD intensified camera to obtain a sequence of eight images (576 x 285 pixels each) in a 15 m/s reacting flow field over a time span of ~88 microseconds. Their technique utilized laser-induced incandescence to measure soot volume fractions in a flame. Although not as fast as the previously mentioned technique, the advantage of their approach was the use of pulsed (~10 nsec duration) Nd:YAG lasers whose output can be more efficiently converted to 2<sup>nd</sup>, 3<sup>rd</sup> and 4<sup>th</sup> harmonics and is used in a large number of existing planar techniques. In both techniques, the speed, resolution

and maximum number of frames of the high-speed camera as well as the flexibility of the laser system were limiting factors.

Overall the previous laser scanning systems were limited by the use of low repetition rate lasers. In the current work we have created a pulse burst laser capable of achieving high repetition rates up to 10 MHz with pulse widths as small as 20 nano-seconds. Also the previously used cameras were limited to low repetition rates and those that could achieve Mhz repetition rates were bulky, expensive and had low resolution. The recent advances in camera technology and laser technology have made imaging at MHz rate feasible at higher resolutions.

#### 1.4 Pulse burst laser systems in high-speed laser diagnostics

A key component of the 3-D imaging system is the pulse burst laser. Therefore, a short background on the history of these lasers is provided here. Pulse burst laser systems allow imaging at higher repetition rate and with greater average laser energy available per image as compared to a fixed duration single pulse from dye lasers. Pulse burst lasers allow flexibility in creation of pulses such that the same laser source can be used along with different scanning and imaging systems. Also, the exposure time of the image can now be determined by the pulse duration instead of the camera shutter exposure time.

Figure 1.2 is the flow diagram of a generic pulse burst laser.

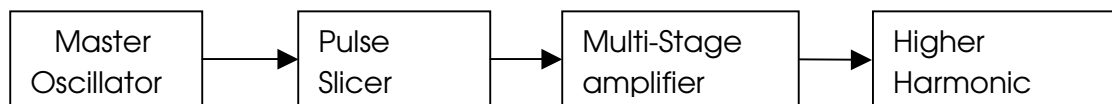


Figure 1.2 Flow diagram of a generic pulse-burst laser system.

One of the earliest pulse burst laser systems was developed by Huntley [1994] and Grace et al [1998]. They developed a repetitively Q-switched laser for holographic applications. The laser could produce a burst of high energy pulses on the order of hundreds of milli-joules. Since Ruby lasers require very high pump energies the operation of that laser was only possible intermittently (on the order of minutes). The use of the laser was thus impractical for several applications.

The development of pulse burst laser systems based on Nd:YAG has proved a compact and efficient way of creating pulses. Nd:YAG has several optical and mechanical properties which makes it ideal for use in pulse burst laser systems. Wu et al [2000] developed a Nd:YAG based pulse burst laser. The laser could produce up to 99 pulses with individual energies in excess of 1 mJ/pulse. Their laser system consisted of a single frequency diode pumped 20mW continuous wave (CW) solid state laser as the base laser. The output from this laser was preamplified by 2500 times in four passes. Pair of pockels cells was then used to “slice” the CW laser into 20 nanosecond pulses with an interpulse period as short as 1 micro-second. These pulses were subsequently amplified by another preamplifier by approximately 13 times before being amplified by a chain of three additional Nd:YAG amplifiers. The gain in these was 10,10 and 8 respectively. The overall gain of the system was  $2.5 * 10^7$ . The pulses then underwent a second harmonic generation (SHG) to green light. They used the pulse burst to visualize shock-wave/boundary layer interaction in a Mach 2.5 flow using filtered Rayleigh scattering. They employed a CCD camera with a resolution of 360\*360 pixels to capture 30 images of the flow at 0.5MHz.

Thurow et al [2004] at Ohio State University improved on this system by developing the 2<sup>nd</sup> generation Nd:YAG based pulse burst laser. The central idea behind the system was once again the use of a Nd:YAG continuous wave (CW) laser as master oscillator and the subsequent amplification of the laser pulses created by a pair of pockels cells. The chief improvement was the addition of a phase conjugate mirror (PCM) which serves the dual purpose of enhancing the contrast ratio and reducing parasitic oscillations by acting as a filter between the earlier and latter stages of laser amplification. This system is capable of creating pulses as short as 10ns with repetition rates of 1MHz. The pulse energies achieved were in excess of 100mJ /pulse. They did not use this laser for high-speed scanning instead; they used the pulse burst laser for MHz rate planar Doppler velocimetry (PDV). They obtained 28 time-correlated realizations of the convective velocity of large scale-structures in compressible axisymmetric jets at 1MHz. At Auburn University we have improved upon the 2<sup>nd</sup> generation pulse burst laser to develop the 3<sup>rd</sup> generation pulse burst laser. The 3<sup>rd</sup> generation laser system is the centerpiece of development of a high-speed 3-D imaging system and is discussed in detail in the next Chapter.

## 1.5 Space and time scales in a flow field

A laser sheet scanning system is designed based on the kind of flow that is to be studied and the kind of data one seeks from the flow. The efficacy of a 3-D imaging system is gauged by its ability to meet the temporal and spatial resolution required to image a desired flow field. A detailed explanation of resolution requirements for 3-D imaging is given by Clemens [2002]. In turbulent compressible high-speed flows the

fluctuations in temperature, pressure and other scalar quantities take place across a range of scales. The largest scale is known as the outer most scale and is denoted by  $\delta$  for example the local width of a mixing layer. The outer-scale evolution occurs over “large-eddy-turnover” time given by:

$$\tau_{os} \approx \frac{\delta}{\Delta U} \quad (1.1)$$

Where,  $\Delta U$  is an outer scale flow velocity variable such as the convective velocity difference across a mixing layer. The smallest scales are where the larger gradients occur. The inner scale evolution time is given by:

$$\tau_{is} \approx (\text{Re}_\delta)^{-1/2} \tau_{os} \quad (1.2)$$

Where,  $\text{Re}$  is the Reynolds number based on outer-scale variables. In addition to evolution time scales, convective time scales also need to be considered. In the case of high velocity flows they may be smaller than the evolution time scales. The convective inner time scale is given by:

$$(\tau_{is})_{conv} = \lambda_v / U_{conv} \quad (1.3)$$

Where,  $U_{conv}$  is the average convective velocity of a mixing layer and  $\lambda_v$  is the strain limited vorticity scale. For example for a flow with flow velocities of 110 m/s and 10 m/s across a 10 cm thick mixing layer  $\tau_{os} \approx 1$  ms and  $\tau_{is} \approx 1.4$  micro-seconds and  $(\tau_{is})_{conv} \approx 300$  nano-seconds. The above example illustrates the variation in time-scales for a given flow and shows the time constraints under which a system might have to

operate. The laser sheet scanning system being developed at Auburn University can achieve repetition rates of up to 10 MHz which means it could acquire 50 images in 5 micro-seconds. This implies that this laser sheet scanning system can image outer scales of flows at higher Reynolds numbers and image inner scales of flows at lower Reynolds numbers.

Spatial resolution must also be considered in addition to temporal resolution. To be able to resolve a particular scale of the flow the volume of the flow imaged on to a pixel should be much smaller than that scale of the flow. Given that there is an inherent tradeoff between the resolution and imaging speed of a camera, the choice of the imaging system becomes a function of the aim of the experiment. Also, it is desired that the dynamic spatial range (DSR) of a 3-D imaging system be large so that a range of scales can be resolved. The DSR of a 3-D imaging system is the ratio of the largest scales to the smallest scales which it can resolve. The DSR required of an imaging system that can resolve all the scales of the flow is equal to the DSR of the flow and is given by the inverse of the following expression [Buch and Dahm 1998]:

$$\frac{\lambda_d}{\delta} = \Lambda \text{Re}_\delta^{-3/4} \text{Sc}^{-1/2} \quad (1.4)$$

Where,  $\lambda_d$  is the strain-limited scalar diffusion inner scale,  $\delta$  is the outer-scale dimension,  $\text{Re}$  is the Reynolds number based on outer flow variables and  $\Lambda$  is an empirically determined constant and  $\text{Sc}$  is the Schmidt number. Su and Clemens [1999] suggested a value of 14 for the constant based on their measurements of finest mass diffusion scales in planar jets. The primary limitation of achieving a high DSR is the

generation and imaging of large number of 2-D sheets. For example for a flow with Reynolds number of 500,000 and Schmidt number of 1 the DSR of the entire flow would be 1343. A DSR of such a magnitude cannot be achieved by the current camera technology and since resolution decreases as camera framing rate increases the DSR would be less for high-speed scanning flow visualization. It is to be noted that the ability of a laser sheet scanning system to resolve scales temporally is limited by the speed of its slowest component. The following chapters describe the characteristics of the components of the high-speed 3-D flow visualization system.

## 2 PULSE BURST LASER SYSTEM

### 2.1 Overview

The development of a flexible, high-speed 3-D laser scanning technique imposes several constraints on the laser source used. 3-D laser scanning of high-speed flows requires that the acquisition time of data be on the order of tens of microseconds. This is due to the fact that high-speed flows move very quickly in and out of the field of view of the imaging system. Also, in order to capture the physical mechanisms within the flow field the acquisition time for a 3-D scanning technique should ideally be an order of magnitude faster than the evolution timescale of the flow structures. These timescales may be on the order of hundreds of microseconds or smaller in turbulent flows and thus the 3-D scan acquisition time should be on the order of tens of microseconds. This means that the laser source being used must be able to provide enough laser energy within a single pulse at MHz repetition rates for the desired imaging. However, thermal loading limits the pulse repetition rates of typical Nd:YAG based lasers to repetition rates of 10-100Hz. This problem is overcome by the pulse burst concept. The idea is to use the laser system at high repetition rates for a short period of time thus keeping the overall duty cycle (average power) low. This ensures that the system is not under excessive thermal stress.

The second constraint on the system was that of flexibility in terms of acquisition speed. We intend to visualize low speed as well as high-speed flows, which implies that the laser source must be compatible with high-speed as well as low speed cameras. The 3<sup>rd</sup> generation pulse burst laser (PBL) system developed at Auburn University's Advanced Laser Diagnostics Laboratory (ALDL) is capable of generating a burst of pulses at a repetition rate of anywhere between 0 – 5MHz.

In addition, previous pulse burst systems required considerable amount of space and were thus constrained to a single location. It was envisaged that this pulse burst laser system would be portable and thus allow the 3-D scanning system to be moved to different locations. The 3<sup>rd</sup> generation laser occupies half the area on an optics table (6 square feet) as compared to the 2<sup>nd</sup> generation laser at Ohio State University and is installed on a movable workstation.

Finally, the laser was designed with the vision of commercializing it in the future. In order to ensure the adoption of this technology it was necessary to keep the overall cost of the system down. Some components used in the current pulse burst system are significantly less expensive than their counterparts in the previous systems. Thus, the pulse burst system was designed to be faster, more flexible, cheaper and more compact than any previously developed pulse burst laser systems.

The design of the new pulse burst laser system at ALDL is based on laser systems previously developed at Princeton University by Wu and Miles [2000] and at Ohio State University by Thurow et al [2004]. Similar systems have also been built recently for NASA [Wernet and Opalski, 2004] and the University of Illinois [Elliot et al.,2005]. The

basic scheme employed in these earlier systems has been that of a master oscillator power amplifier (MOPA), where a burst of pulses is formed initially at low power and subsequently amplified through a chain of flashlamp pumped power amplifiers. The master oscillator consists of a low power (20 – 100 mW) continuous wave (cw) Nd:YAG laser operating at 1.064 microns. Nd:YAG is an acronym for neodymium-doped yttrium aluminium garnet;  $\text{Nd:Y}_3\text{Al}_5\text{O}_{12}$ . It is a crystal that is used as a lasing medium for solid-state lasers. Nd:YAG lasers have a greater thermal loading to fracture thereby permitting higher repetition rates of laser pulsing. Nd:YAG has hardness of mild steel and is a robust material that allows polishing to high quality finish. It has a narrow linewidth and other appropriate optical properties which make it ideal for use in pulse burst laser systems. Also a Nd:YAG source can be conveniently converted to 2<sup>nd</sup> and 4<sup>th</sup> harmonics which makes the laser useful for various applications.

The cw laser beam from the master oscillator is then preamplified and double-passed through a pair of Pockels cells, which are used to slice the cw laser beam into a burst of low energy pulses. Following formation of the low energy burst of pulses, the pulses are passed through a series of flashlamp pumped Nd:YAG rod power amplifiers with an overall system gain of  $10^5$  to  $10^8$ , resulting in pulse energies ranging from 1 – 100 mJ/pulse. These pulses may then be frequency doubled, also called as second harmonic generation. This allows availability of light energy at frequencies useful for diverse practical applications. The pulse burst laser system at ALDL is similar to the above systems except for two significant changes which allow it to achieve sufficient energy within a single pulse while meeting all the constraints mentioned above.

The first change is to the pulse slicing mechanism, which in the Ohio state university pulse burst system developed by Thurow et al [2004] was conducted using a pair of Pockels cells. Commonly used for Q-switching, Pockels cells are electro-optic devices that cause polarization retardation to a laser beam when a high voltage (several kV) is applied. For the formation of short duration pulses, the high voltage signal to the electro-optic crystal must be cycled on and off very rapidly. While the rise time can be kept to the order of 3-5 nsec, the fall time on the pulse is greater than 50 nsec. This necessitates the use of a 2<sup>nd</sup> Pockels cell to form a fast falling edge for the pulse, thus allowing pulse durations of 10 nsec. This process can be repeated quite rapidly, thus allowing for a burst of pulses to be formed with pulse spacing as short as 1  $\mu$ sec (1 MHz). In general, a pair of Pockels cells and associated electronics must be custom built and can be quite expensive (>\$50k). In this new pulse burst laser system, a more economical (~\$5k) acousto-optic modulator is used for pulse slicing.

The 2<sup>nd</sup> change involves the pumping of the Nd:YAG amplifier rods using Xenon flashlamps. In earlier systems, the gain of the amplifier system varies with time (i.e. gain curve) appearing as a Gaussian shaped profile in time with a width of 100 – 200  $\mu$ sec. The gain curve is then superimposed on the burst of pulses resulting in a non-uniform distribution of energy over the pulses. The problem is exasperated further during the latter stages of amplification, where the gain stored in the rods is depleted by the passage of each pulse. In addition, this limits the application of the laser as pulses are confined to a 100 – 200  $\mu$ sec window. For the new pulse burst laser system, the gain curve has been modified to have a more uniform ‘top hat’ profile with an effective length of 1 msec. This results in a more uniform amplification of pulses which would be

advantageous in many diagnostic applications. The pulse burst laser system at ALDL consists of two main elements. The first is the pulse slicing mechanism and has been described in the next section 2.2. The second is the power amplifier chain and is discussed in section 2.3.

## 2.2 Pulse Slicing Mechanism

Pockels cells were replaced by an acousto-optic modulator (AOM) in the current system. This was done not only because the latter was 10 times cheaper but also because Pockels cells and the associated high-speed/high-voltage electronics is not readily available as an ‘off-the-shelf’ system and must be specially designed and built for the current application. Also, the high voltage electronics present some safety and reliability concerns and would not be easily replaceable in the event of failure. Lastly, the original manufacturer of the Pockels cells used in the previously discussed systems is not in business and there would be some additional risk associated with trying a new design. The next section discusses the working principle of the AOM and the important design parameters of the AOM relevant for the current application.

### 2.2.1 AOM Concept

The Acousto-Optic Modulator, also referred to as Bragg cell, operates on the principles of the acousto-optic effect, where an acoustic wave traveling through a crystal or liquid causes a small variation in the index-of-refraction. This variation appears to an optical beam passing through the medium as a sinusoidal grating with wavelength equal to the acoustic wavelength. The incoming beam of light is split up into various beams of light. These beams of light are referred to as different orders. The number of orders and

their orientation depends on the material properties of the AOM, the angle of incidence of the beam of light and the propagation characteristics of the light beam and sound. Figure 2.1 is the representation of a typical acousto-optic interaction.

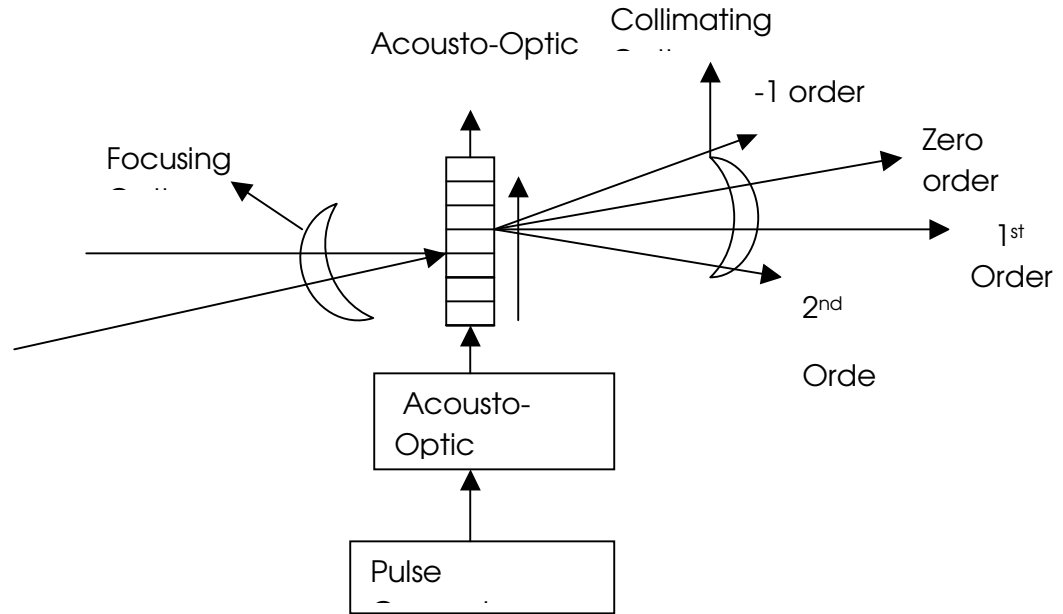


Figure 2.1 Schematic of a typical AO interaction. The sound wave propagates in the upward direction whereas the laser beam propagates obliquely towards the right.

Study of acousto-optic interaction was first done by Leon Brillouin in 1922 who studied acousto-optic interaction in weak sound fields. The epochal work in the field was done by Raman and Nath [1935-1936] who calculated the amplitude and hence the energy of various orders. The behavior of acousto-optic interaction (AOI) has been successfully described by calculating the integral effect of the orthogonal interaction of a sound field and an electromagnetic field. Both heuristic analysis of AO interaction based on wave theory and a rigorous formal treatment based on Feynman diagram/path integral formulation is presented in a book titled “Acousto-Optics” by Adrian Korpel [1997].

Even though AOI has been studied extensively it was not until the development of lasers that the practical use of AOM's was realized. Light is chargeless and massless and researchers were looking for a way to manipulate the direction of light propagation. AOMs offered a safe and inexpensive option. AOM's have been used as Q-switches which are on-off devices internal to a laser cavity and useful in producing high pulse energies at low repetition rates. AOM's have also been used as switches in the communication industry. A laser beam passing through an acousto-optic material undergoes a frequency shift equal to the acoustic frequency of the sound wave it interacts with. This frequency shift offers a sensitive way of measuring distance and velocity. By varying the frequency of the acoustic waves the laser beam can be deflected in different directions. Such a device is called an acousto-optic deflector (AOD).

The selection of acousto-optic material is the most critical part of AO design and it depends on the application being pursued. Some examples include gallium phosphide, tellurium oxide and silicon dioxide. Once the AO material is selected, it is optically polished. The side of the material is coated to reduce optical reflections. This is to reduce optical losses. A transducer is then bonded to the side of the AO material. Typically metal bonding or epoxy bonding is used for this purpose. The transducer which is a piezoelectric material converts RF energy supplied to it to acoustic energy. The design of the AOM used in the current application is discussed in the next section. Figure 2.2 is a photograph of the AOM used in this study.

Most AO devices operate in the Bragg regime, where most of the incident light can be diffracted into the 0<sup>th</sup> and 1<sup>st</sup> order with the remaining modes annihilated by

destructive interferences. This form of diffraction is most efficient at the Bragg angle,  $\theta_B$ , given by:

$$\theta_B = \frac{\lambda F_a}{2V_a} \quad (2.1)$$

where  $\lambda$  is the wavelength of light in air,  $F_a$  is the acoustic frequency and  $V_a$  is the acoustic velocity. By modulating the intensity of acoustic waves, via a piezoelectric transducer bonded to the crystal, the amplitude of the deflected light can be controlled.

For the current application, we are interested in slicing pulses of light from a cw laser beam. This can be done by rapidly turning the deflection of the laser beam ‘on’ or ‘off’ via manipulation of the acoustic waves inside the AO crystal. In this case, the deflected laser beam constitutes the desired burst of pulses with the beam only being deflected when a positive voltage is applied to the AOM driver. As we are interested in the formation of short duration (as short as 10 nano-secs) pulses, the most important properties are the rise/fall time, diffraction efficiency and contrast ratio of the AOM and driver.

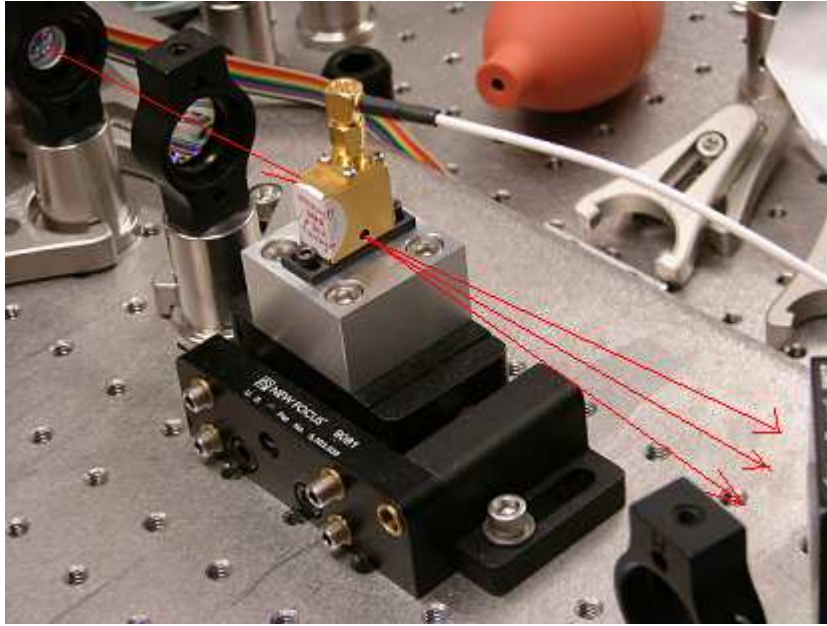


Fig 2.2 Photograph of an AOM with the arrows indicating different orders in which a beam of light is split up.

The rise time,  $t_r$ , of the deflected pulse is primarily limited by the time it takes for the acoustic wave to travel across the aperture of the beam and is given by:

$$t_r = \frac{D}{V_a} \quad (2.2)$$

where  $D$  is the diameter of the focused beam within the AO medium. With acoustic velocities on the order of several thousand meters per second, rise times of a few nanoseconds can be achieved by tightly focusing the beam inside the crystal. Additional factors that can affect the rise time of the laser pulses are the intensity profile of the incident beam (e.g.  $TEM_{00}$ ) and the speed of the AOM RF driver and pulse generator. The pulse generator creates a TTL signal and is used to drive the AOM RF driver. Since all electronic instruments have an inherent rise time they too contribute to the overall rise

time of the pulse. In this work, a rise time of ~10 nsec has been achieved and is comparable to the 3-4 nsec rise times achieved with Pockels cells. It is important to note that if the beam is too tightly focused it might damage the AO material. Thus the AO material chosen must have a high enough damage thermal threshold.

The transmission efficiency of most AO materials is around 90%. The diffraction efficiency is proportional to the acoustic power, figure of merit of the optical material, geometric factor of interaction and inversely proportional to the square of the wavelength. AOM diffraction efficiencies can range from 30 – 90% depending on the AOM design. This low efficiency is not a major issue in the design of the pulse burst laser system since the AOM is not being used as an intra-cavity device; thus, the loss in efficiency is not exponential. Also the pulse slices would be greatly amplified later by the amplifier chain

Lastly, the contrast ratio of the AOM is another important parameter and is given as:

$$CR = \frac{I_{on}}{I_{off}} \quad (2.3)$$

where  $I_{on}$  is the maximum intensity of the laser pulse and  $I_{off}$  is the intensity of laser light with the AOM turned nominally off. The contrast ratio is important because any light passing through the amplifiers when the slicer is nominally ‘off’ will be amplified. Because the slicer is off much longer (by ~3 order of magnitude) than it is on, this can cause a significant loss of the energy stored in the amplifiers and limit the energy gained by the pulses. The intensity of light when the AOM is turned off is primarily caused by

impurities in the crystal, scattered/diffracted light from various optics in the system and leakage RF power from the modulator driver. Typical AOMs have CR ranging from 500 to 1000, which is similar to that achieved using Pockels cells. The CR can be increased by spatially filtering the diffracted laser beam, which helps minimize the contribution of scattered/diffracted light, and using a modulator driver with high extinction.

### 2.2.2 Pulse Slicing

Figure 2.3 below is a schematic of the pulse slicing mechanism. A continuous wave Nd:YAG laser (CrystaLaser model IRCL-100-1064-S-0.5%) produces a 0.45 mm beam at 100mW output power. The beam then passes through a Faraday Isolator, which prevents light from reflecting back into the laser cavity. This beam is then focused to a ~0.04 mm spot within an acousto-optic modulator (AOM) using a -15mm concave lens followed by a +35 convex lens. The separation between lenses is approximately 60 mm and the convex lens is about 66 mm away from the AOM. The AOM (Brimrose GPM-400-100-1060) is mounted on a stage that provides both rotation and translation so that the focused spot can be positioned with the AO crystal with an incident angle equal to the Bragg angle.

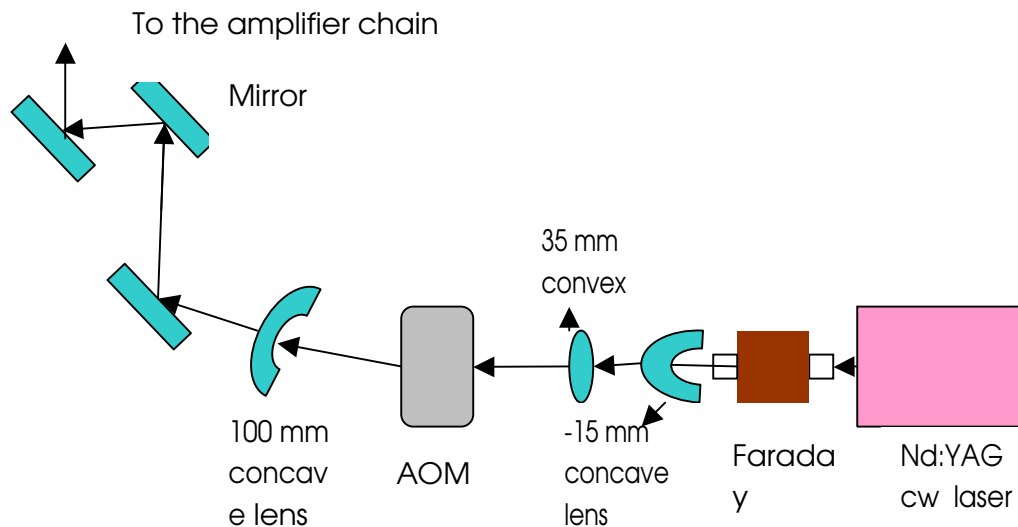


Figure 2.3 Schematic of the pulse slicing mechanism using acousto-optic modulator

The AO crystal is Gallium Phosphide, which has an acoustic velocity of 6300 m/s. This gives a calculated minimum rise time of  $\sim 6$  nsec according to Eq 2.2. Gallium Phosphide has high diffraction efficiency for a wavelength of 1064 nm. It also has a damage threshold of greater than  $5 \text{ W/mm}^2$  which is enough for the current application. The acoustic wave propagates at 6300m/s at a frequency of 400MHz across the AOM and Gallium Phosphide is ideal for use in high frequency signal processing devices. The acoustic wave within the crystal is powered by a 1.5 W, 400 MHz RF Source (Brimrose FFA-400-B2-F1.5-X). It has a specified rise time of 3.5 nsec and an extinction ratio  $>50$  dB. The modulation is controlled via an externally applied TTL signal (Quantum Composers 9514+,  $\sim 3$ nsec rise time) and has a digital modulation bandwidth of DC-5 MHz. Thus, bursts with repetition rates as high as 5 MHz are possible. When turned on, approximately 60% of the energy is in the 1<sup>st</sup> order with the 0<sup>th</sup> order blocked by a beam block. The resulting burst of pulses ( $\Delta\theta = 67\text{mrad}$ ) is collimated by a +100mm focal

length lens to a diameter of 3.3 mm so that they are slightly diverging. This is done so that the diverging beam expands at a rate optimum to “fill” the laser rods in the amplifier chain. Three mirrors are used to direct the beam into the amplifier chain.

### 2.2.3 Post AOM pulse characteristics

Figure 2.4 shows oscilloscope traces for pulses ranging from 10 to 50 nsec in duration (FWHM). The waveforms were acquired with a high-speed photo detector (Thorlabs DET210) with a quoted rise time of 1 nsec on a 500 MHz oscilloscope (Tektronix TDS5054B). The photo detector was placed after the +100mm collimating lens and the waveforms represent the general nature of the pulses that will be seen by the power amplifier chain. The peak power was estimated to be 56 mW by measuring the power when the beam is continuously deflected by the AOM. For the short duration pulses shown in Figure 2.4, the power rapidly rises during the 1st 15 nsec of the pulse formation. After that point, the power continues to rise at a reduced rate until it levels out at ~40 mW. It is not clear if this slow increase in power between 15 and 35 nsec is optical in nature or an artifact of the measurement technique.

The use of an AOM to produce laser pulses adds an additional layer of complexity to the measurement as one must account for the acoustic wave traveling across the aperture of the beam. To capture the entire spatial extent of the pulse, light must be focused onto the active area of the detector. As a result, the linearity limit of the detector was exceeded, making accurate amplitude measurements difficult with the current set-up. Regardless of these issues, the measurements shown in Figure 2.4 still reveal the most important features of the pulses, namely, the duration and approximate shape of the pulse.

The measured rise/fall time of the pulses is approximately 10 - 15 nsec, not accounting for the slow signal increase between 15 and 35 nsec. This agrees well with an expected rise time of ~8 nsec when the rise time of the pulse generator (3 nsec), modulator driver (3.5 nsec) and acoustic velocity (~6 nsec, Eq. 2.2) are taken into account. The approximate energy in each pulse can be determined by integrating the power with respect to time. The energy contained in each pulse is estimated to be ~0.3, 0.7, 1.1, 1.6 and 2.0 nJ for the 10, 20, 30, 40 and 50 nsec pulses, respectively.

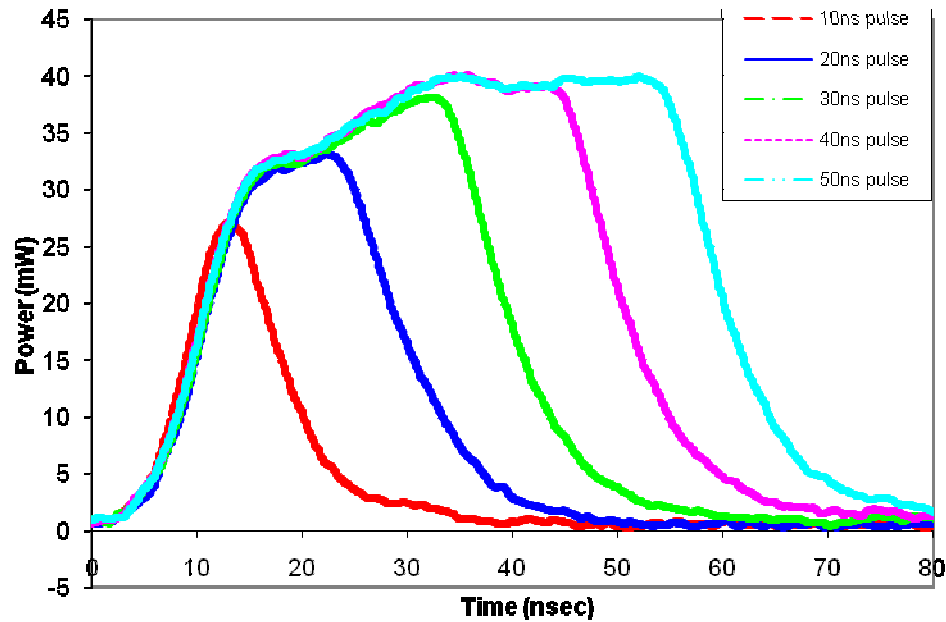


Figure 2.4 Pulse shape for 10, 20, 30, 40 and 50 nsec duration pulses.

The formation of pulses by the AOM can be repeated at repetition rates up to 100 MHz. The high repetition rate capabilities of the current system are demonstrated in Figure 2.5, which displays a burst of four 20 nsec long pulses separated in time by 200 nsec each (5 MHz), with the repetition rate limited by the pulse generator and not the AOM. Higher repetition rates should be possible with more capable pulse generators. A

more practical bursts of pulses for fluid dynamic measurements is shown in Figure 2.6, which depicts a bursts of 100 pulses separated by 10 microseconds each (100 kHz). This repetition rate is suitable for many transonic and supersonic flow fields. The total duration of this burst is 1 msec, which corresponds to the duration of the gain envelope of the power amplifier chain.

The contrast ratio of the pulses was determined by measuring the power with the AOM turned off and the cw laser turned on. A Coherent LM-2 VIS power detector with sensitivity as low as 10 nW was used to detect the small amount of laser light that leaks through when the AOM is off. The energy post AOM with the AOM on was measured to be 55mW ( $I_{on}$ ) and the energy post AOM with the AOM off was measured to be 2.36 micro watts (uW) ( $I_{off}$ ). As the measurements were moved “downstream” in the optical arrangement the contrast ratio improved. This improvement is attributed to the fact that the light coming through with the AOM off is due to scattering of the laser beam by the impurities in the crystal. Since the scattering is off-axis, it tends to diverge with distance and is further reduced by various optical instruments in the optical path. Spatial filtering is typically used to boost the contrast ratio, however it also decreases the useful energy ( $I_{on}$ ). The contrast ratio post spatial filter was earlier measured as 15000:1 however; the contrast ratio was later measured to be 20000:1 without the spatial filter. In the current application spatial filtering is not necessary since the contrast ratio is already high. This is another advantage since spatial filtering is a tedious process requiring careful alignment and isolation from jitters.

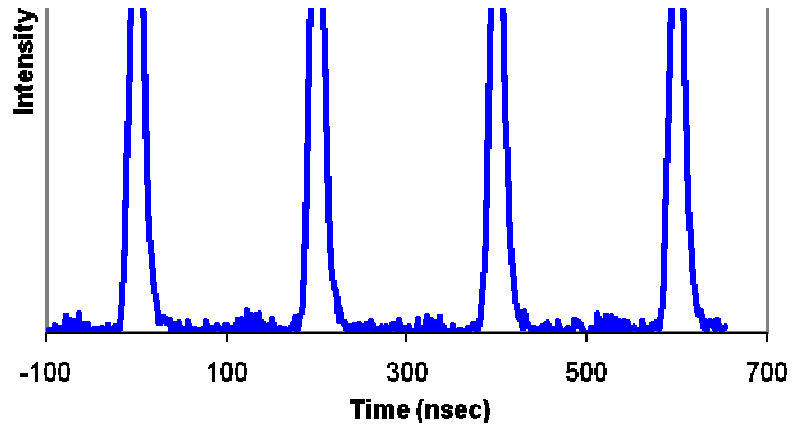
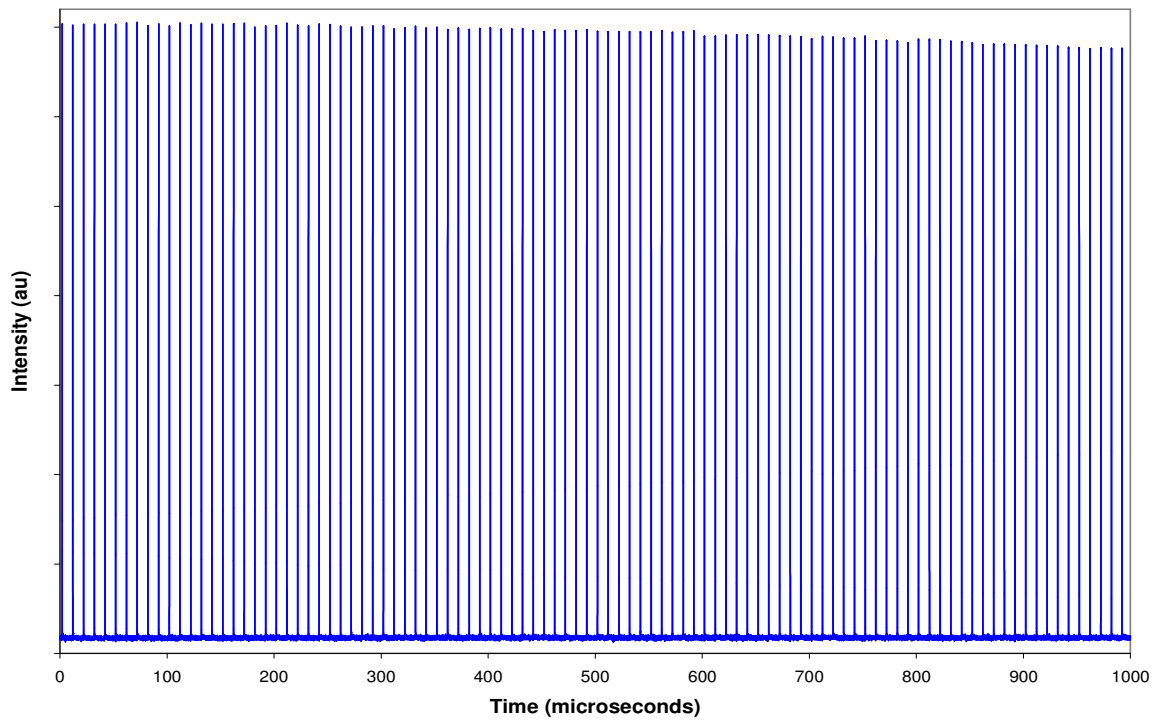


Figure 2.5 A burst of four 20 nsec pulses separated by 200 nsec each (5 MHz).



2.6 Oscilloscope trace of a 100 pulse burst of pulses at 100 KHz. Each pulse is 20 nsec in duration.

Figure

The principal advantage of the AOM pulse slicer is its flexibility. The duration of pulses and the pulse spacing is determined by a TTL voltage applied to the AOM driver. Using a computer based timing card and pulse generator, the user has maximum flexibility in determining the properties of the pulses, such as their timing and duration. In many applications, it is desired to have uniform energy contained in each pulse. The flexibility to change the pulse duration from pulse to pulse may be used to attain this goal where the pulse duration can be increased with time to offset the gain loss occurring in the system. Alternatively, many applications, particularly those associated with transient phenomena, will benefit from the ability to operate in an asynchronous fashion. With the 1 msec window of gain available, it should also be possible to synchronize the laser with random, external events that occur within that window.

### 2.3 Laser Amplifier Chain

The burst of pulses must be amplified by a factor of  $10^6 - 10^8$  to be useful for the fluid dynamic measurement applications envisioned. Amplification by a factor of  $10^7$  would yield 10 milli-joules (mJ) of energy for a 1 nJ 20ns pulse. A power amplifier chain was built as a custom design by LaserPath Technologies (Oveida, FL) to provide a gain of  $10^7$  over a 1 msec period. Unfortunately, technical difficulties with the high voltage power supply have resulted in sub-optimum performance of the 1<sup>st</sup> amplifier.

Specifically, for the measurements reported here, it was not possible to operate the first amplifier at maximum power. Rather, the power was limited to ~5-10% of the design capability. Thus, a complete characterization of the laser system is left for future work. The current measurements, however, do illustrate the overall concept and function of the amplifier system and are an essential step in the development of the system.

The amplification system consists of a water chiller, flashlamp power supply and the amplifier breadboard including three flashlamp-pumped double-pass Nd:YAG rod amplifiers, beam alignment optics and the cooling lines. The water chiller and the flashlamp power supply are housed in the flashlamp controller. Figure 2.7 is a schematic of the optical layout of the amplifier chain. Figure 2.8 is the photograph of the overall layout of the pulse burst laser and figure 2.9 is the photograph of the amplifier chain. The arrows in the figures indicate the direction of beam propagation and lines with arrows in both directions indicate a double pass of the beam.

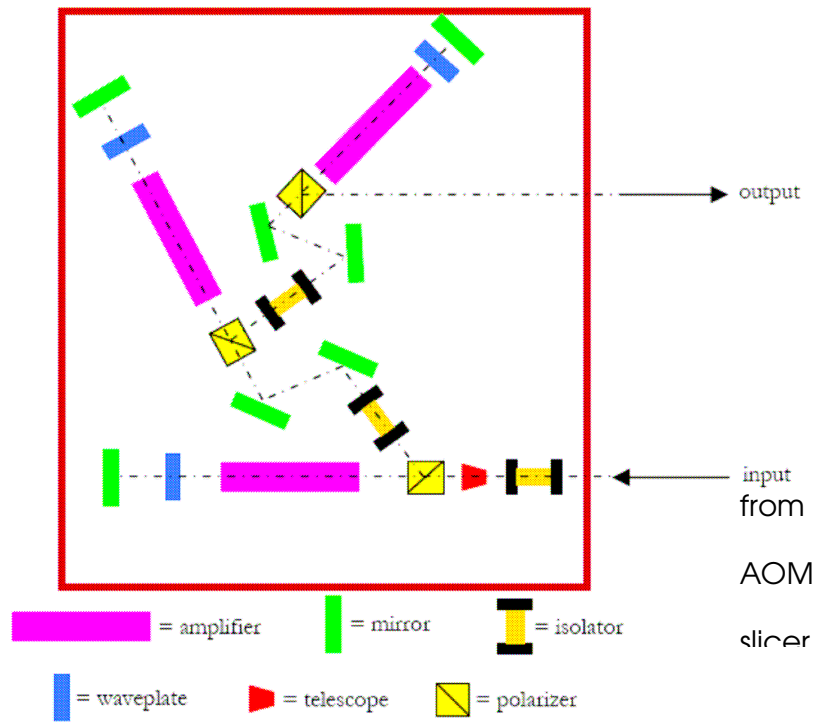


Figure 2.7 Schematic of power amplifier chain for AU pulse burst laser system.

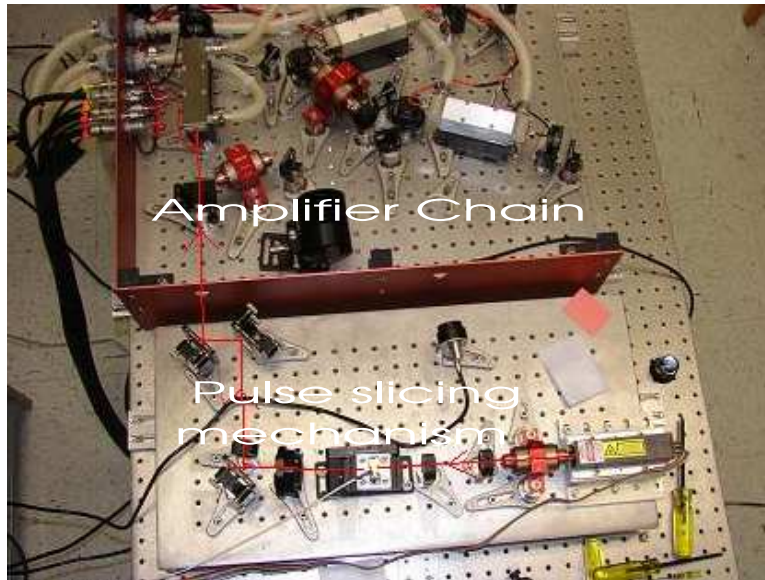


Figure 2.8 Photograph of the overall layout of the pulse burst laser system

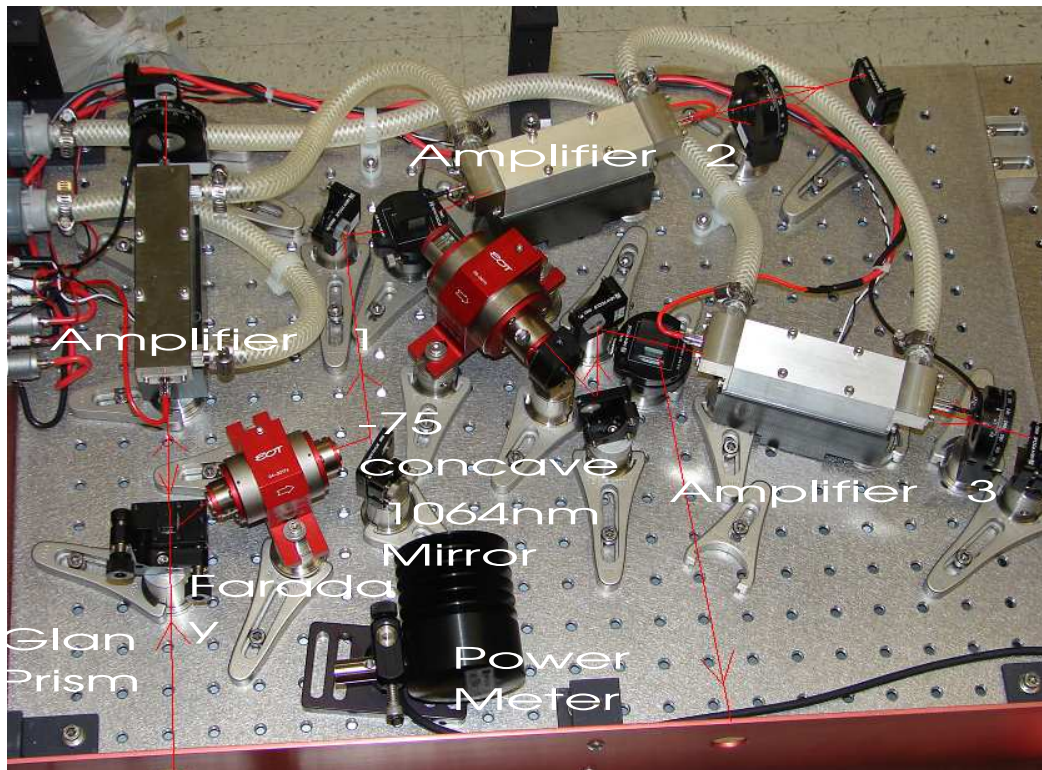


Figure 2.9 Photograph of the amplifier chain with the main components labeled. The lines with arrows pointing in both directions indicated double pass of the beam before entering the glan prism.

Each laser amplifier consists of a Xenon flashlamp and Nd:YAG laser rod housed in an optical pump chamber. The Xenon flashlamp emits broadband radiation which reflects off of the walls of the elliptical pump chamber and is focused at the center of the Nd:YAG rod. The rods are 4 by 100 mm (diameter by length), 5 by 100mm and 6.3 by 100mm, respectively. The Nd:YAG crystal absorbs radiation mostly in the bands between 730-760 nm and 790-820 nm. The remaining energy is wasted and leads to thermal heating of the Nd:YAG rod. This energy must be removed by circulating chilled water through the amplifier system. The electrical energy supplied to the flashlamps is created by the flashlamp power supply.

The power supply provides electrical pulses at a repetition rate of up to 10Hz. It does so using an electronic pulse forming network (EPFN). The maximum electrical energy per pulse is 20, 30 and 40 Joules respectively scaling up as the diameter of the gain crystals. A slightly divergent beam with a horizontal polarization is first passed through a glan prism un-deflected and then through the 1<sup>st</sup> amplifier and a quarter wave plate. The beam then undergoes reflection and double passes through the 1<sup>st</sup> amplifier and the quarter wave plate. As a result of the double pass through the quarter wave plate the polarization of the beam is rotated by 90 degrees to a vertical orientation. The beam reaches back to the Glan prism but owing to vertical polarization, is deflected towards the second amplifier. Glan prisms are made of birefringent materials, they are used to control the direction of laser beam propagation since they preferentially transmit or reflect a laser beam depending on the polarization of the laser beam.

Faraday Isolators are used to isolate the amplifiers in order to avoid parasitic oscillations of photons between the amplifiers. This parasitic oscillation too gets

amplified and thus robs the laser pulses of gain. The beam double passes across the 2<sup>nd</sup> and the 3<sup>rd</sup> amplifier similar to the 1<sup>st</sup> amplifier. After the 3<sup>rd</sup> amplifier, amplified pulses are then directed to KTP crystal where they are converted to green light. This process is referred to as second harmonic generation (SHG). Conversion to second harmonic or higher harmonics opens up the possibility of using the laser for a wide range of fluid dynamic diagnostics.

Thermal lensing was a major issue in the current application. It occurs due to the non-uniform heating of the gain medium. This typically causes some transverse gradient of the refractive index. It can also lead to thermal stresses which may further increase the transverse gradient or bulge the rod. All the above mentioned changes lead to focusing of the beam which can be dangerous to other optical instruments. A beam focused within an amplifier would experience significantly less gain vis-à-vis a beam which is “filling” the amplifier. In order to counteract thermal lensing a -75 mm concave lens was placed just before the 3<sup>rd</sup> amplifier and a concave mirror right after it. As a result of this arrangement the beam size is optimized for amplification and it emerges collimated post 3<sup>rd</sup> amplifier.

The most significant change to the AU pulse burst laser’s amplifier chain compared to earlier systems is the temporal gain curve of the amplifier chain. In previous designs, the power supply for the amplifiers was similar in design to those used in standard single-pulse Nd:YAG lasers, which did not have high repetition rate capability. As such, these systems delivered a Gaussian shaped gain curve with duration from 100-200  $\mu$ sec. The energy within a pulse would thus depend on its temporal location within this period of time. For the pulse burst laser concept, this

curve is superimposed on the burst of pulses making it difficult to achieve uniform energy over the entire burst of pulses. In the current design, the desired gain curve is 1.0 msec long with a uniform gain over 600 microseconds (us) of that duration. The gain was calculated by measuring the power of a 20ns pulse (FWHM) before and after amplification. The power was measured using a high-speed silicon photo detector (Thorlabs DET210) which outputs a voltage that is proportion to incident laser power. The voltage was observed on an oscilloscope, which allowed for observation of the pulse shape as well. It should be noted that the detector is only linear up to approximately 100 mV at which point the detector begins to saturate.

Figure 2.10 presents the gain profile at 1.064 microns of the second amplifier along with the electrical trigger signal. The maximum gain measured for the second amplifier was 134, however, the photo detector saturated and thus the true gain is expected to be higher than the values indicated above. As can be seen in fig 2.10 after an initial rise time of ~550  $\mu$ sec post trigger, the gain profile of the amplifier is fairly uniform over a 600 us time span.

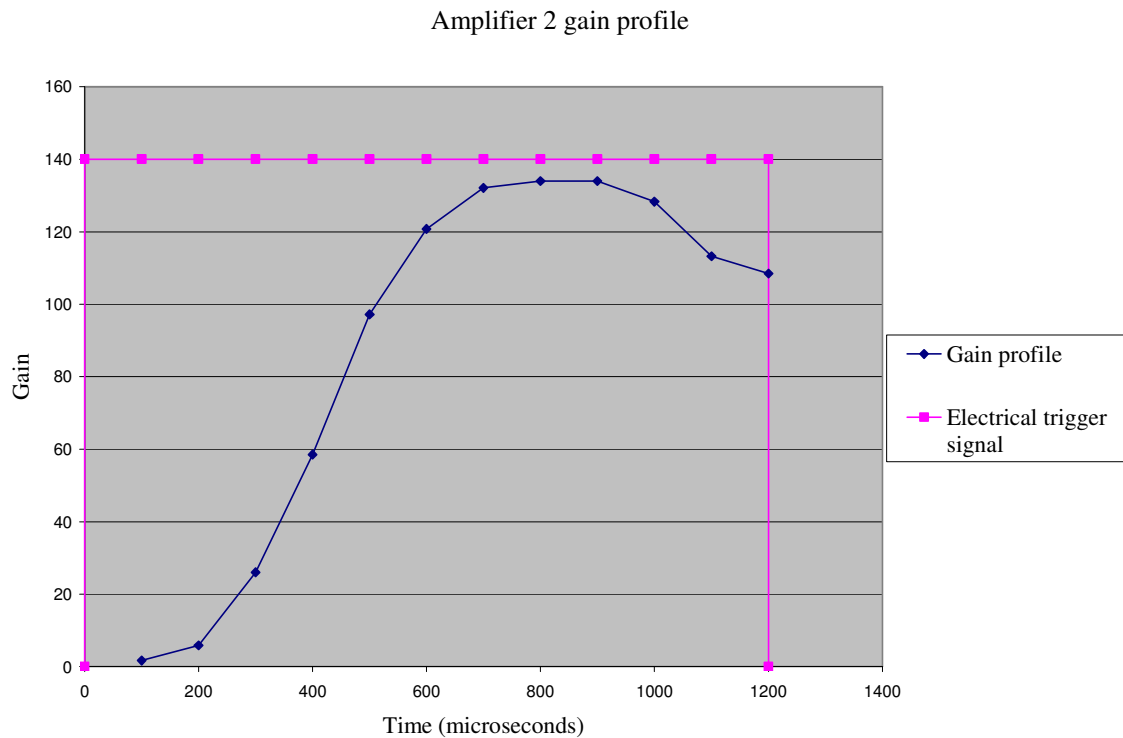


Figure 2.10 Oscilloscope trace of the gain profile of the 2<sup>nd</sup> amplifier with time on the X axis and gain on the Y axis along with the electrical trigger signal.

This increased uniformity of the gain curve has been achieved by modifying the pulse forming network that regulates current to the flashlamps. A more uniform gain curve is significant as the non-uniformity of pulses has been a problem in the past, particularly when using harmonic frequencies, which have a non-linear conversion efficiency. The extension of the gain envelope to 600 us is also quite significant in that it will allow for operation at lower repetition rates while still producing a significant number of pulses. For example, operation at a “low repetition rate” of 10 kHz would have been limited to 2-3 pulses in previous designs. In the current design, 10-11 pulses with significant energy are expected for operation at 10 kHz. This will allow the laser system to be used in a broader range of fluid dynamic applications, which may require

lower repetition rates, more pulses, or both.

As mentioned, the 1<sup>st</sup> amplifier in the amplifier chain deviated from the intended performance. The cause for this erroneous performance is currently under investigation but believed to be contained in the electronic power supply provided with the system. The unit is currently being repaired. The 1<sup>st</sup> amplifier exhibits much lower overall gain and operates intermittently at high power settings. The maximum gain observed post 1<sup>st</sup> amplifier was 16 whereas the anticipated gain was 200 thus the malfunction of the 1<sup>st</sup> amplifier result in pulse energies an order of magnitude less than expected.

Figure 2.11 shows the cumulative gain in pulse energy of a 20ns pulse (FWHM) after it passes through the 1<sup>st</sup> and 2<sup>nd</sup> amplifier. The amplifier gains are multiplicative. Given that the maximum gain of the 1<sup>st</sup> and 2<sup>nd</sup> amplifier is 16 and 134 respectively theoretically we expect a gain of approximately 2100. However, the maximum gain in figure 2.11 was measured to be 1050. This is partially due to the fact that the photo-detector measuring the gain saturated when the pulses were amplified in the peak gain regime. We thus expect the true combined gain to be significantly higher than that observed. Also the gain profile in fig 2.11 is more non-uniform than the individual gain profiles. This is attributed to the disparity in the gain profiles of the 1<sup>st</sup> amplifier and 2<sup>nd</sup> amplifier.

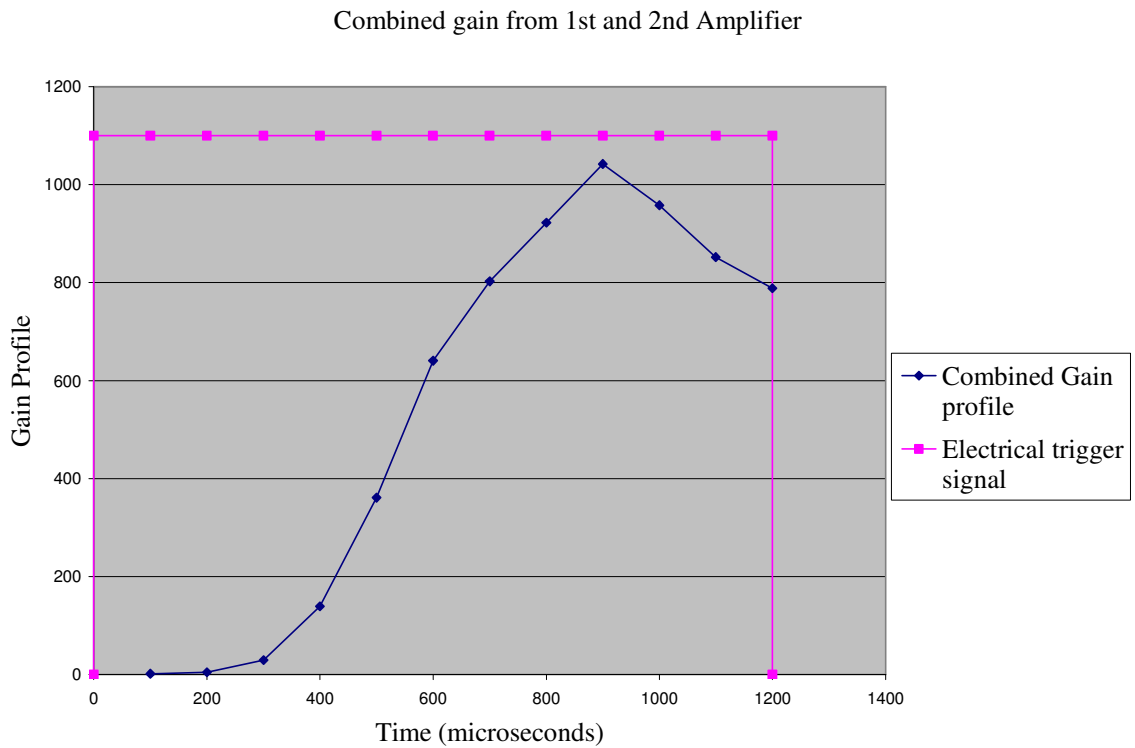


Figure 2.11 Oscilloscope trace of the combined gain from the 1st and the 2nd amplifier on the Y axis with time on the X axis along with the electrical trigger signal.

An important aspect of amplification is the retention of pulse shape characteristics. Figure 2.12 shows the oscilloscope trace of the pulse shapes prior and post amplification. The trace show a slight change in the shape of the pulse after amplification however the shape of the pulse is still Gaussian indicating faithful reproduction of pulse shape.

### 20ns FWHM Post and Pre Amplification

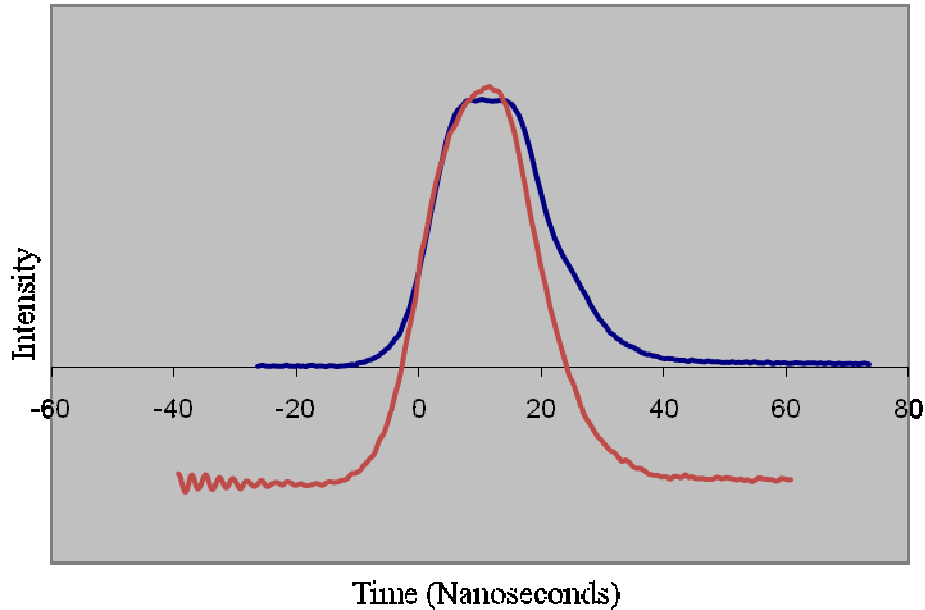


Figure 2.12 Oscilloscope trace of a 20ns pulse shape pre and post amplification. The squiggle which is on the pre-amplified pulse is due to certain EM interference from another device.

#### 2.4 Pulse Burst Laser Conclusions

The combined energy gain of all three amplifiers could not be measured due to the failure of the power supply. Also as a consequence of the malfunction it is not possible at the present time to obtain data on the uniformity of energy amongst pulses. Still, the current measurements show that the fundamental concept of the amplifier system is effective in creating amplified pulses with low parasitic oscillations. The measurements show that it would be possible to easily obtain greater than 100 pulses at up to 5MHz repetition within 20 microseconds. This allows the laser to be used flexibly with different imaging systems.

Further characterization of the pulse burst laser would include sending multiple pulses with variable pulse widths and then observing the variation in the amplification

amongst them. This process would be repeated at different repetition rates and at different delays from the electrical trigger signal to get a complete idea of the capability of the system.

### 3 HIGH-SPEED SCANNING AND IMAGING SYSTEMS

#### 3.1 Overview

The main theme of this thesis is the development of a high-speed 3-D flow visualization technique. Two techniques that have been used in the past for 3-D flow visualization are tomography and holography. However these techniques require complicated optical arrangements and are difficult to implement. The third option that has been used by researchers is laser scanning. The central idea of laser scanning is to scan a sheet of laser across a flow field. The interaction of the laser sheet and the flow field results in scattering or fluorescence. This scattering or fluorescence is then imaged on to a camera which is used to obtain 2-D “slices” of the flow field. Figure 3.1 is a schematic of the 3-D laser scanning method. In the schematic below the burst of pulses is incrementally deflected at small angles across the flow field. A cylindrical lens expands the beam in a single direction.

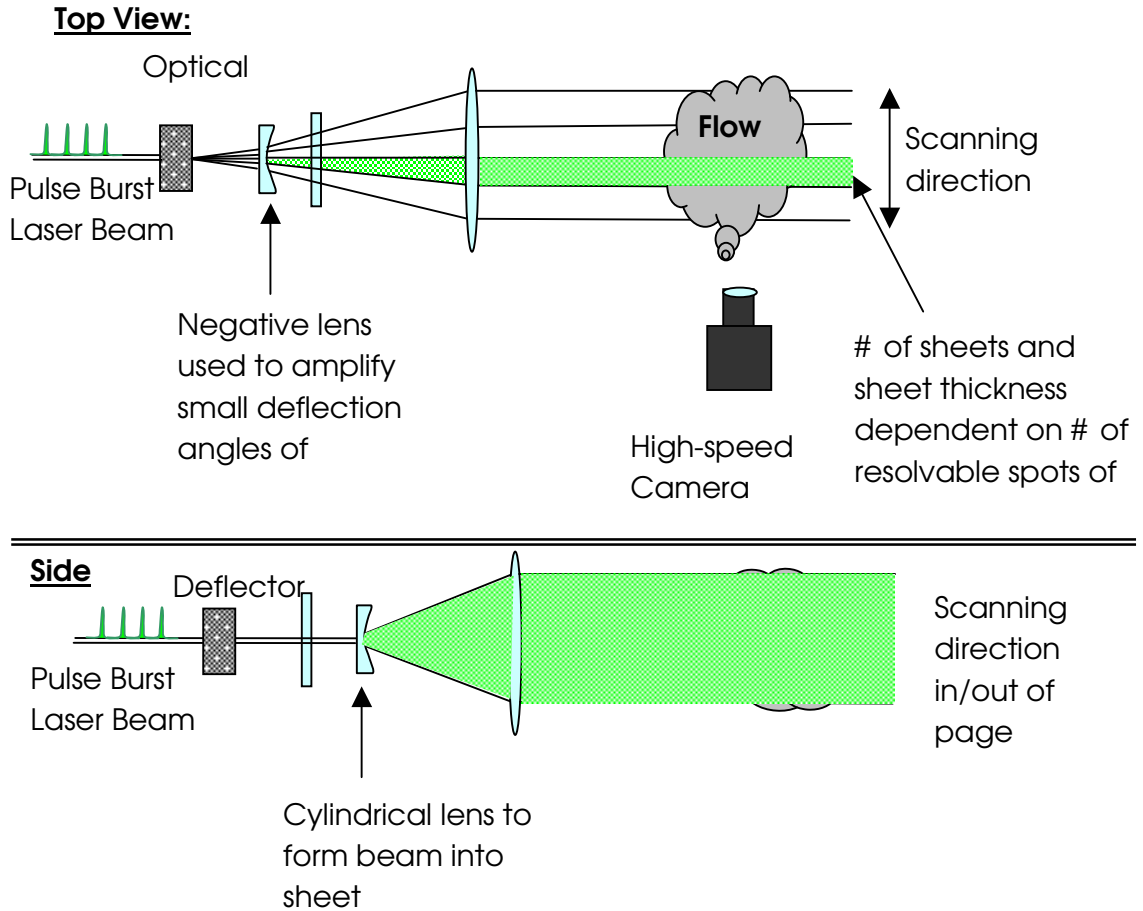


Figure 3.1 Schematic of proposed volumetric flow measurement system.

The key components in 3-D imaging are the high-repetition rate burst of pulses, the scanning mechanism and the high-speed camera. The pulse burst laser system has been described in detail in chapter 2. This chapter describes the remaining components of the 3-D flow visualization system: the high-speed deflector and the high-speed camera. Section 3.2 of this chapter discusses the most important parameters in the selection and design of a beam deflector for laser scanning. Section 3.3 provides information about various methods of optical scanning and reports results obtained using an acousto-optic

deflector and a galvanometric scanning mirror. Lastly, Section 3.4 describes the imaging system being used at Auburn University's advanced laser diagnostics laboratory (ALDL).

### 3.2 Scanning system parameters

Some of the earlier efforts at obtaining 3-D flow measurements used mechanical translation of the laser. As one might imagine, the acquisition of information took substantial amount of time due to the slow speed of physical translation. Also, such measurements were tedious to obtain. Since then, scanning systems have become more sophisticated mainly due to microprocessor/electronic control of the scanning system. The performance of an optical scanner can be characterized by the number of resolvable spots, the deflection efficiency, the slew rate and the random access time.

The number of resolvable spots,  $N$ , is the number of discrete angles, or positions, that the scanner can access over its full range. The number of resolvable spots is given by:

$$N = \frac{\Delta\alpha}{\Delta\phi} \quad (3.1)$$

where  $\Delta\alpha$  is the total deflection angle of the device and  $\Delta\phi$  is the total angular spread of the incident beam. The natural divergence for a collimated laser beam of wavelength  $\lambda$  and diameter  $D$  is given by:

$$\Delta\phi = \frac{\lambda}{D} \quad (3.2)$$

where  $\lambda$  is the wavelength and  $D$  is the beam's diameter [Laufer, 1996]. Thus, each laser pulse must be deflected by at least  $\Delta\phi$  in order to obtain a distinctly new position.

The slew rate characterizes the rate at which the deflection angle can change and can be represented by an angular velocity or number of spots accessed per unit time. The slew rate must be high for high-speed 3-D scanning. In the current application the pulse burst laser can create pulses at up to 10 MHz thus we need a scanner which can produce 10 resolvable spots per microsecond (10 spots/micro-second) to achieve the full potential of the system.

The random access time is the time it takes for deflector to go from one arbitrary position to another arbitrary position. Fast slew rates do not guarantee a short random access time. This is apparent in the case of mechanical deflectors which due to inertia take a longer time to reverse directions but can obtain high speeds in a single direction. Short random access times may be important for PIV or time resolved 3-D measurements; however, as one would need to obtain 3-D images of the same flow region in rapid succession.

The scanner should have high deflection efficiency. This is of importance as it ensures that most of the laser energy is used for measurements and is not wasted. Wasted laser energy means more amplifiers are needed in the pulse burst laser system to get the required power for fluid dynamic measurements. Addition of amplifiers increases system complexity and increases the overall costs.

In the selection of a suitable scanner, the capabilities of the overall system must be considered. For example if the framing rate of the camera being used for imaging is 1 MHz over 32 frames then the scanner should be able produce at least 32 resolvable spots at a slew rate of 1 spot per microsecond (i.e. 1 MHz). High optical damage thresholds,

ability of the device to be electronically triggered and cost are other important parameters that must be considered.

### 3.3 Various scanning systems

The scanning systems are distinguished on the basis of their working principle. The scanning systems that may be potentially used are electro-optic deflectors, acousto-optic deflectors and rotating/galvanometric scanning mirrors.

#### 3.3.1 Acousto-Optic deflectors

An acousto-optic deflector (AOD) works on the same principle as an AOM, that is the acousto-optic effect. This effect arises when an acoustic wave traveling through a crystal or liquid causes a small variation in the index-of-refraction. This variation appears to an optical beam passing through the medium as a sinusoidal phase grating with wavelength equal to the acoustic wavelength. The light is diffracted, where the angle of diffraction is proportional to the frequency of acoustic waves. Thus, by modulating the acoustic frequency, via a piezoelectric transducer bonded to the crystal, the deflection angle of light can be controlled. When operated in the Bragg regime, the majority of incident light can be directed into the 1<sup>st</sup> order. The deflection efficiency of the AOD in most applications is the same as the 1<sup>st</sup> order diffraction efficiency of the AOD. This may vary by as much as 50% across the entire scan angle since there is a unique Bragg angle for every different frequency of the acoustic wave. Since the direction of beam propagation into the AOD remains fixed the diffraction efficiency varies.

The number of resolvable spots an AOD can make depends on its bandwidth.

Combining equation 3.1 and 3.2 we get:

$$N = \frac{\Delta\alpha * D}{\lambda} \quad (3.3)$$

For an AOD total deflection angle ( $\Delta\alpha$ ) is equal to:

$$\Delta\alpha = \frac{\lambda * BW}{V} \quad (3.4)$$

Where,  $V$  is the acoustic velocity within the device and BW is the bandwidth of the acoustic-optic RF driver. The random access time,  $t$ , of acousto-optic devices is defined by the time it takes for an acoustic wave to pass across the beam aperture. It is defined as:

$$t = \frac{D}{V} \quad (3.5)$$

Where,  $D$  is the beam aperture in the acoustic direction and, in this case, the same as the diameter of the laser in equation 3.2.

Combining equations 3.3, 3.4 and 3.5 we get:

$$N = BW * t \quad (3.6)$$

The time taken by the AOD to deflect the laser beam from one end can be significant if the change in the driving frequency change is in the form of a step function. If the frequency change is done stepwise the total deflection time would be the product of the number of spots and the random access time. Allowing the frequency to vary, such as

would be produced by ramp input (e.g. frequency chirp), can produce faster scans, but introduces a cylindrical lensing effect, which can be modeled and accounted for as shown in equation 3.7 below. In the case of a ramp input the total scan time would be significantly less than the product of the number of spots and the random access time. This is because the random access time is calculated assuming that the acoustic frequency is constant across the entire beam. The other effect of providing a ramp input would be reduction in the total number of resolvable spots as described by the equation below:

$$N = \left(1 - \frac{t}{T}\right) \left(t \times \frac{BW}{1.34}\right) \quad (3.7)$$

Where, BW is the bandwidth of the RF driver, T is the total scan time and t is the random access time. Here it can be seen that the number of resolvable spots decreases as the scan time is decreased (i.e. as the rate is increased).

The most common acousto-optic material is Tellurium Dioxide ( $\text{TeO}_2$ ), which has a high acousto-optic figure of merit. Specifications for one commercially available device indicate that an AOD constructed from  $\text{TeO}_2$  could achieve 32 resolvable spots with a total scan time of 1.27 microseconds, well within the required range for the current technique. The manufacturer, however, had concerns about the use of this material with short duration, high intensity laser pulses and suggested fused silica as an alternative. This is particularly of concern as the incident beam must be reshaped and focused into the device to get maximum efficiency. Fused silica has a much higher damage threshold and can be used at UV wavelengths, making it suitable for use with 3-D UV fluorescence measurements, whereas  $\text{TeO}_2$  is limited to wavelengths greater than 400 nm. AODs

using a fused silica crystal are reasonably priced (order of a few thousand dollars) relative to other components in the 3-D flow visualization system.

To verify the high-speed operation of the AOD, the output from a standard frequency doubled Nd:YAG (New Wave Research) laser operated at  $\sim 5$  mJ/pulse was focused into the AOD with a 100 mm cylindrical lens, producing a 2 mm wide elliptical spot within the crystal. Figure 3.2 is a photograph of the set-up. The AOD was constructed of fused silica with a 6 x 1 mm aperture with the acoustic direction along the major axis. The speed of sound within the AO medium is 5960 m/s, which corresponds to a  $\sim 1$   $\mu$ sec random access time for a 6 mm aperture. Acoustic energy was provided by a 4 W RF driver with frequency tuning from 75 to 125 MHz.

The aim of doing the experiments was to measure the number of resolvable spots which could be obtained using the AOD. Also it was desired to determine the time taken by the AOD to deflect the laser pulse from one extreme position to another. The output of the Nd:YAG laser had an angular spread of  $\sim 1.4$  mrad, which is five times the diffraction limit for a 2 mm beam (see Eq. 3.2). The angular spread of the beam was calculated by imaging the beam at a certain distance and then using trigonometric identities to determine the divergence of the beam. The number of resolvable spots observed were  $\sim 4$ -5, which is consistent with Eq. 3.1. Resizing the beam to a 6 mm aperture and precisely collimating it would have produced a greater number of spots, but the appropriate lenses were not available in time for these experiments. The speed of the device was determined by providing a step command to change the device frequency from 75 to 125 MHz. The limiting factor was the AO driver's finite response time to the step input. It was found that the beam could deflect from the starting position ( $f = 75$  MHz) to the end

position ( $f = 125 \text{ MHz}$ ) in  $\sim 10 \text{ } \mu\text{sec}$ . Thus, according to Eq. 3.7, over 33 spots over the 10  $\mu\text{sec}$  sweep should be possible with a properly collimated input.

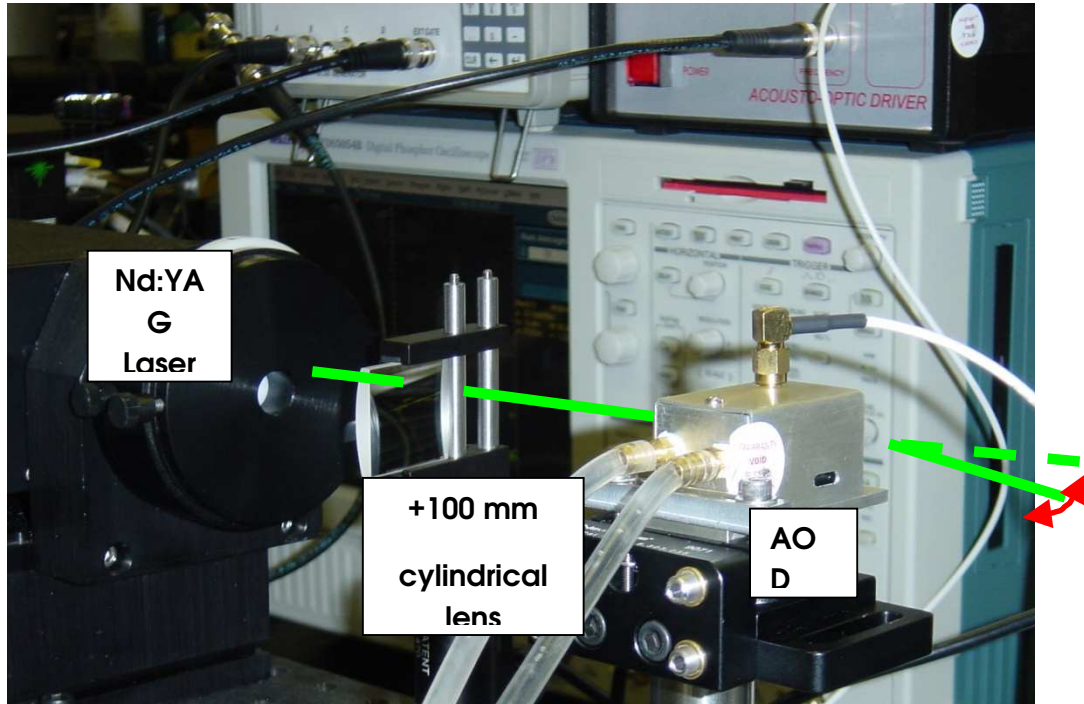


Figure 3.2 Photograph of acousto-optic deflector experimental set-up.

As indicated by the measurements above, the AOD could be used for up to 3MHz repetition rate imaging but would not be able to produce enough resolvable spots for faster speeds. In addition, expanding the capabilities of AODs to a higher number of resolvable spots is somewhat limited. The biggest drawback to AODs, however, is that the deflection efficiency ranges from 35 – 65% across the entire range of deflections angle for the specified application. This is significant due to limited laser power and camera sensitivity at high-speeds. In addition, expanding the capabilities of AODs to a higher number of resolvable spots is somewhat limited.

### 3.3.2 Electro-Optic deflectors

Electro-optic deflectors are commonly found in laser q-switches. They are able to precisely deflect a beam using the electro-optic effect where the index of refraction of a crystal varies with applied voltage. The access time is limited by the passage of an electromagnetic wave across the beam aperture, thus allowing much higher deflection speeds than can be achieved with an acousto-optic deflector. Deflectors with 20 MHz bandwidth (random access time of 50 nsec) are commercially available with deflection efficiencies greater than 90%, an important factor in applications where pulse energy is critical.

The primary limitation of electro-optic deflectors is their cost. To achieve usable deflection angles (and therefore a large number of resolvable spots), these devices require voltages on the order of kV. In general, electro-optic deflectors are driven towards small apertures because the deflection sensitivity is inversely proportional to the square of the aperture. One commercially available deflector recommends a 0.3 mm diameter beam size, which drives  $\Delta\phi$  to 1.78 mrad. With a sensitivity of approximately 5 mrad/kV, 32 resolvable spots would require a ~12 kV high-speed driver. The small beam size would also make optical damage a concern, thus necessitating a larger aperture device and therefore much larger drive voltages. While this may be technically feasible, it would also be quite expensive when compared to the alternatives. Also high voltages raise safety concerns and careful handling of this equipment is a must. Still, there may be some unique applications where this approach is desirable.

### 3.3.3 Rotating/Galvanometric scanning mirrors

Scanning mirrors are another alternative for high-speed laser scanning. The primary advantage of these over AOD's are their high deflection efficiency (>98%). Rotating mirrors may be driven by an electric or gas turbine drive or a galvanometer. For turbine driven mirrors, the mirror continuously rotates at high-speeds; whereas, in the case of a galvanometer, the rotation is restricted to a finite angle. The speed and response time of a rotating mirror is dictated by the mirror inertia, balance and tuning of the system. Rotational speeds up to 20,000 Hz using gas turbine drives have been realized in practice and have found use in some models of ultra-high-speed cameras (e.g. Cordin Camera). A 500 Hz rotating mirror was used by Patrie et al [1994] in their 3-D imaging work. The main drawback to a rotating mirror is the slow response time of the mirror to an external command due to the angular momentum of the mirror. This makes it difficult to the time the mirror's position with an external event (e.g. passage of a turbine blade, rotation of a crankshaft, etc.) and limits the flexibility of the system. An additional problem, with respect to the pulse burst laser system, is that the mirror must be in the starting scan position sometime within the 1 msec gain window of the amplifier system. This can be circumvented somewhat by using a multi-faceted polygonal mirror; however, this adds complexity to the system and variations in the manufacturing of each mirror surface can cause jitter in the position of the laser sheet.

For the current application, a galvanometric scanning mirror (General Scanning Inc. VM500) was used to deflect pulses. This type of mirror was used in a similar high-speed application by Hult et al. [2002] and was found capable of achieving high scan speeds. Figure 3.3 contains a photograph of the mirror (GSI Lumonics VM500) along

with the 15 mW HeNe laser used to characterize the mirror. A servo (GSI Lumonics MiniSAX) was used to control the mirror with power provided at +/- 15 V using a variable DC power supply (Tenma 72-7245). A positive (+) and negative (-) terminal, with respect to ground, is essential for proper operation of the device. The mirror was controlled by a +/- 3V command input generated using LabView software and a National Instruments data acquisition board (Model 6251). An optical encoder built into the mirror provides feedback of the mirror's position. The mirror is AR coated for 532 nm with reflectivity of over 98%. The maximum scan angle for the mirror is +/- 20 degrees. Figure 3.4 shows the plot of scan angle vs command input (volts). This figure indicates the linear relationship between the command input and the scan angle.

An important consideration in high-speed scanning is the time taken for the mirror to move from one position to the next (i.e. random access time) as well as its angular velocity (i.e. slew rate). Figure 3.5 shows the response of the mirror to a step command telling it to move its position from  $-13^{\circ}$  to  $+13^{\circ}$ . The waveform shown in the figure, including the notch that occurs at a time of 1,000 microseconds, was confirmed by imaging the position of a moving laser spot with the high-speed camera. As can be seen, the mirror takes over 1 msec to settle into its final position, indicating a random access time of over 1 msec. The overshoot is less severe for smaller step angles where the settling time is less than 1 msec. For high-speed 3-D imaging, where the mirror does not have to stop at each position, the slew rate is the more relevant parameter to consider. In this case, laser pulses will be deflected while the mirror remains in motion. As the laser pulses are short ( $\sim 20$  nsec), the position of the mirror for that image is effectively constant.

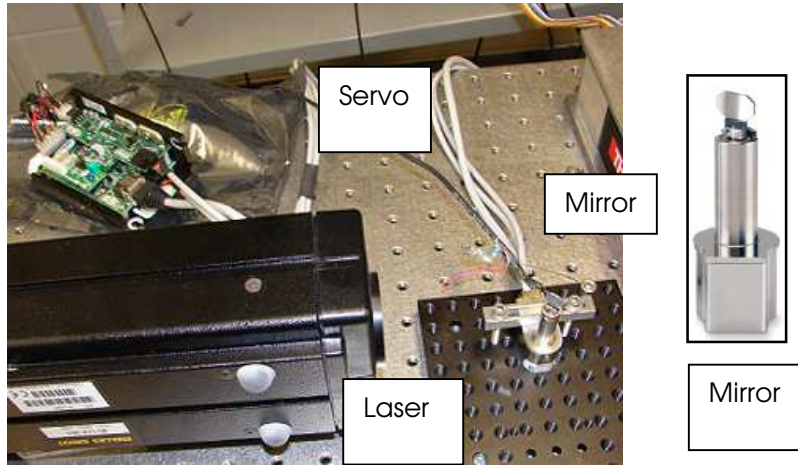


Figure 3.3 Schematic and photograph of experimental set-up of laser and scanning mirror.

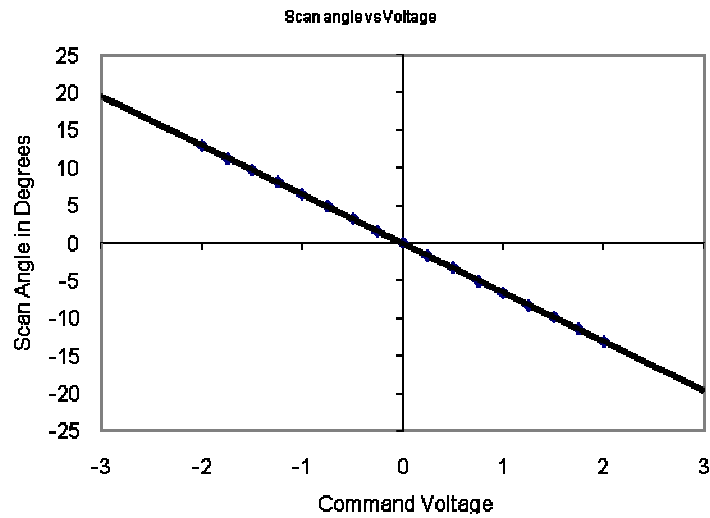


Figure 3.4 Scan angle vs command input voltage.

The instantaneous speed of the mirror can be estimated by calculating the slope of the curve in Figure 3.5. This was done using a polynomial curve fit, which made

calculation of the derivative somewhat easier. This is shown in Figures 3.6a (curve fit) and 3.6b (slope).

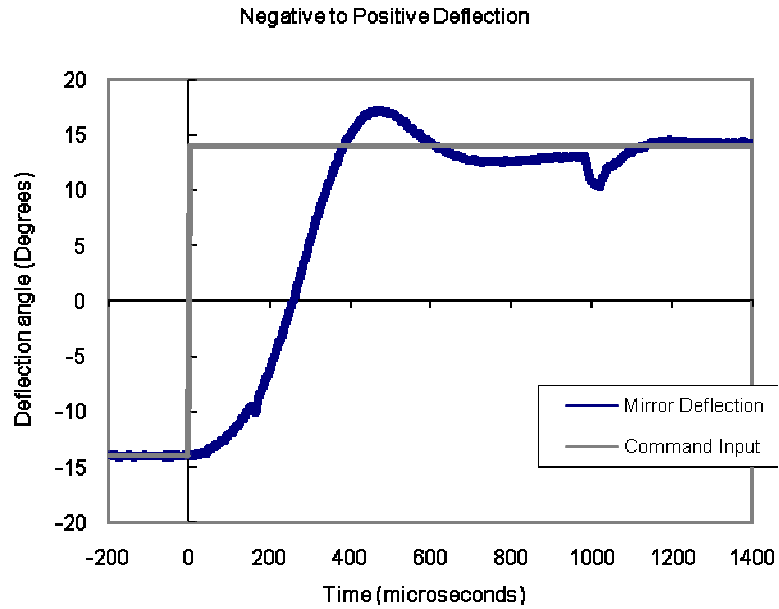


Figure 3.5 Response (deflection angle) of mirror to a step input command.

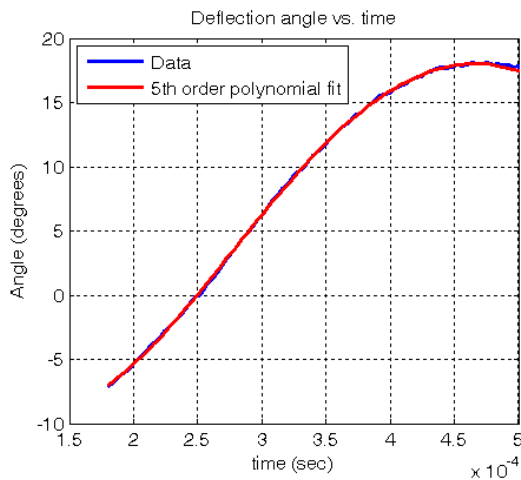


Figure 3.6a Polynomial curve fit to data shown in Fig. 3.

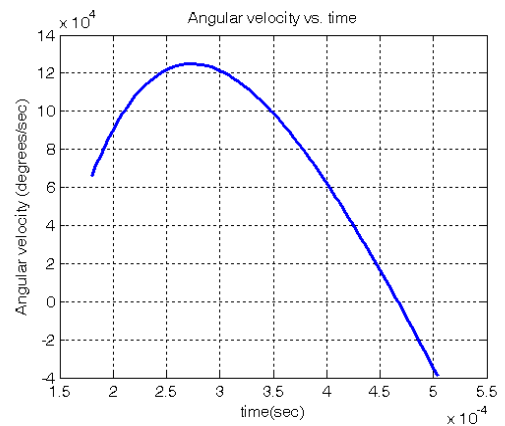


Figure 3.6b Angular velocity vs. time for a step input command

Fig. 3.6b shows that the angular velocity of the mirror exceeds 100,000 deg/sec over a time period lasting  $\sim 150 \mu\text{sec}$  with a maximum speed of  $\sim 125,000 \text{ deg/sec}$ . Over this time span, the mirror moves approximately 17 degrees. For a 6 mm diameter Gaussian beam at 532 nm, this range corresponds to  $\sim 2700$  resolvable spots with an average slew rate of  $\sim 18$  spots per microsecond. This is an important observation as it clearly shows that the speed of the mirror is sufficient for very high-speed imaging applications where we would like to acquire multiple planes of data in a few microseconds. In this case, the speed of the mirror is sufficiently fast to acquire 18 planes of data per microsecond. The speed of the mirror can be controlled by modifying the waveform of the command input to a ramp instead of a step or using a smaller step. A large step is necessary in order to allow the mirror to accelerate to high-speeds and was chosen in this case to produce the fastest motion of the mirror.

The repeatability of the waveform shown in Figure 3.5 was determined by imaging a moving spot produced by the laser beam with the high-speed camera. For a fixed time delay after the step input was given, any movement of the spot from its expected position in the image could not be observed, indicating that the motion of the mirror is very repeatable from one command input to the next. Overall, the mirror proves to be a fast, inexpensive, reliable and an efficient scanning system for volumetric imaging.

### 3.4 High-Speed imaging systems

The last component necessary to construct the 3-D imaging system is a high-speed camera. The framing rate of the camera depends upon the number of images one wants to see of a particular event. For 3-D imaging of high-speed flows, the required framing rate may be 10 million frames per second or higher. Until recently, the number of ultra-high-speed cameras commercially available was quite scarce and a limiting factor for researchers trying to develop high-speed imaging technique. Fortunately, a large number of ultra-high-speed cameras capable of framing rates on the order of 1 MHz are now commercially available.

For the current 3-D flow visualization system, a DRS Hadland Ultra68 high-speed camera has been used. This camera combines multiple high-speed imaging concepts to obtain 68 images with a resolution of  $\sim 240 \times 240$  pixels at up to 500,000 frames per second. It is also capable of burst framing rate of up to 100,000,000 frames per second in 4 frame bursts. The camera allows exposure times of 10ns to 1ms per frame. Figure 3.7 is a photograph of the DRS Hadland Ultra68 high-speed camera.



Fig 3.7 Photograph of DRS Hadland Ultra 68 high-speed camera.

The high framing rates are achieved by a novel image capturing process in the camera. Light entering the camera is directed along four different paths using a unique four-way beam splitter. Each image is then formed on one quadrant of the surface of a segmented intensifier, with the firing of each quadrant being independently controlled. The intensifier is attached to a masked CCD (charge coupled device) in which only one out of every 17 pixels is exposed to the light; the remaining pixels serve as on-chip charge storage bins, which allows the camera to be operated at higher frame rates than possible if the image were read out off of the chip. The four-way beam splitter continues to cyclically rotate the light direction over the 4 quadrants until a sequence of 68 images has been captured.

The beamsplitter, intensifier and CCD mask, which divides the signal and limits the fill factor, add a significant amount of noise to each of the images. The gain of the intensifier, however, is sufficient to overcome this noise with the camera performing quite well in poorly illuminated conditions. However, due to the magnitude of the image noise, the camera is unsuitable for quantitative measurements. Also the camera being used is a multi-CCD camera; consequently variations in properties from one sensor to the next can introduce errors, particularly for intensity dependent measurements such as fluorescence based species concentration. These errors can be removed through proper calibration and post-processing of the images, but some effort will be required to identify the noise sources and develop efficient and appropriate calibration and post-processing schemes.

Preliminary estimation of “dark noise” and “white noise” was made during this work. Dark noise as defined by Clemens [2002] is the current that is generated due to the random thermal motion of the molecules on the photo detector of the camera. Dark noise can be estimated by obtaining an image with the camera shutter closed and then calculating the average intensity on the CCD pixels finally recording the image. The average intensity of the dark image was calculated to be 2.1475 with the standard deviation amongst the CCD pixels equaled 0.3752. The average intensity here is a measure of the “dark noise” and it is desired that this value be as small as possible. The “dark noise” may be reduced by cooling the CCD. We also estimated “white noise” which is caused due to statistical fluctuations in the generation of photoelectrons on the photo detector given that the object being imaged is homogenous, white and has been illuminated uniformly. In order to calculate the “white noise” an image of a dot card was

taken and a small location corresponding to 12\*12 pixels was chosen between the black spots of the dot card. Photograph of the dot card is shown in figure 4.7. The average intensity of the chosen area was calculated to be 118.2 whereas, the standard deviation amongst the 12\*12 pixels was found to be 9.3938. The standard deviation in this case represents the “white noise” and the average intensity the desired signal. Thus, the signal to noise ratio is approximately 12.58. These estimates are a crude estimation of the fidelity of the imaging system and a much deeper analysis would be required for error estimation in order to extract an image which is an accurate representation of the flow volume being imaged. The error estimation would be even more significant if this qualitative imaging technique is to be extended to a quantitative measurement tool.

Another issue that must be addressed and can pose a problem is the depth-of-field (DOF) of the imaging system. With 3-D images, the camera must capture images at varying distances from the camera for a single optical setting. A first order approximation of the DOF in a typical imaging system is:

$$DOF \approx 2f_{stop} C \frac{M + 1}{M^2} \quad (3.8)$$

where  $f_{stop}$  is the f-stop of the lens (i.e.  $f/\#$  4),  $C$  is the size of the circle of confusion (i.e. minimum resolvable spot due to defocus) and  $M$  is the magnification. From this equation, it is clear that the DOF is proportional to the image resolution ( $C$  being the smallest feature). The DOF can be improved by reducing the aperture of the lens (increasing  $N$ ), but this will result in lower signal levels due to a decreased solid angle for light collection. As an example, assuming  $M = 0.5$ ,  $C = 1/64''$ , and  $DOF = 1''$ , a lens with  $f/\#$  of 5.3 or greater will have to be used to ensure properly resolved images. If the  $f/\#$  is

increased too much ( $>16$ ), however, the image resolution can become diffraction limited as opposed to DOF limited. The primary concern is the lost signal when operating at increased  $f/\#$ . This puts a greater strain on the power of the laser system, the efficiency of the deflector and the sensitivity of the camera. The effect of this restriction will vary depending on the technique being applied. Techniques like PIV can withstand some amount of defocus and still produce accurate results, while other techniques depend on accurately resolving the flow field.

The variation in depth-of-field during imaging also leads to a variation in the number of photons imaged per pixel. This is assuming that the focal length remains fixed. However, it is possible to calibrate and eliminate this image to image fluctuation. The implementation of the 3-D imaging systems and application of some of these corrective measures is the subject of the next chapter.

## 4 LOW SPEED 3-D FLOW VISUALIZATION EXPERIMENTS

### 4.1 Motivation

The previous chapters have described the essential components of the flow visualization system. In order to gain experience with 3-D imaging and test the effectiveness of the galvanometric scanning mirror and the high-speed camera a series of low speed 3-D flow visualization experiments were conducted. The other reason for doing low speed imaging was the unavailability of pulse burst laser due to technical problems in its power supply. Several other experimental setups to gain experience with high-speed imaging were also tried, including bursting of hand held balloons and imaging of Mie scattering from moisture emitted by a humidifier. However, the best results were obtained by imaging the Mie scattering from incense smoke. Section 4.2 describes the experimental setup in detail and section 4.3 discusses the post-processing of images and the results obtained.

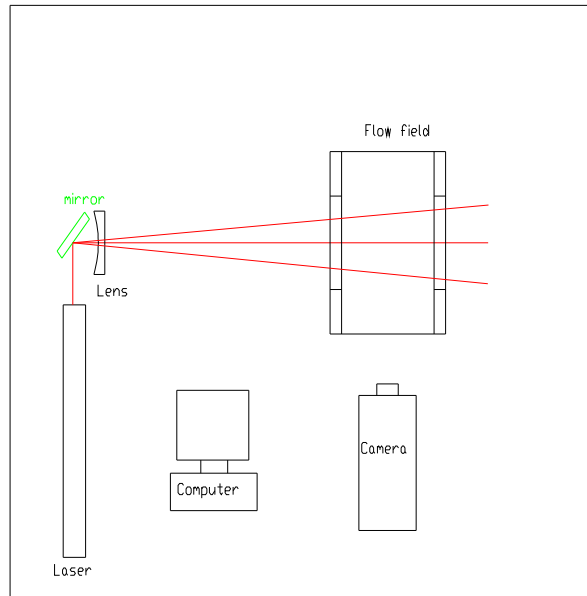


Figure 4.1 Schematic of the experimental set-up of laser and scanning mirror.

## 4.2 Experimental setup

Figure 4.1 is a schematic of the experimental setup. In the low-speed configuration, light from a 15 mW continuous wave (CW) He-Ne laser was substituted for the pulse burst laser. The laser light was then deflected by the galvanometric mirror across the flow field. Figure 4.2 is the photograph of the experimental setup. A cylindrical concave lens was used to convert the laser beam into a laser sheet. The flow field was naturally convecting (i.e. rising) smoke created from four incense sticks. This flow field proved to be a simple yet effective way of creating interesting low-speed flow features with which the 3-D imaging system can be tested. It should be noted that the primary function of the incense smoke was to provide a flow field for demonstrating the concept of the 3-D flow visualization system. Thus, the focus of this work is on the diagnostic techniques as opposed to a detailed investigation of the flow itself. Figure 4.3

is a photograph of the incense sticks used to create the flow field. The flow velocity of the incense was estimated to be less than 1m/s by observing the movement of smoke with the laser sheet held at a fixed location. The camera was located approximately 24 inches away from the center of the flow field. The image sequence constituted of 68 images. Each image corresponded to 3.8" x 3.8" (field of view). The images were across 3.1" in depth the first image to the last. Thus the overall volume of the imaging region being 3.8" x 3.8" x 3.1". The lens used to capture the image sequence was a Nikon 50mm fixed focal lens with a f number of 1.4 and the focal length was 50mm.

Mie scattering from the relatively large smoke particles produced sufficient signal to be detected by the camera even with the relatively low power laser. The sequence of images obtained by the camera were then saved on to the hard drive of a computer where they could then be post-processed to obtain 3-D images and movies of the flow field.

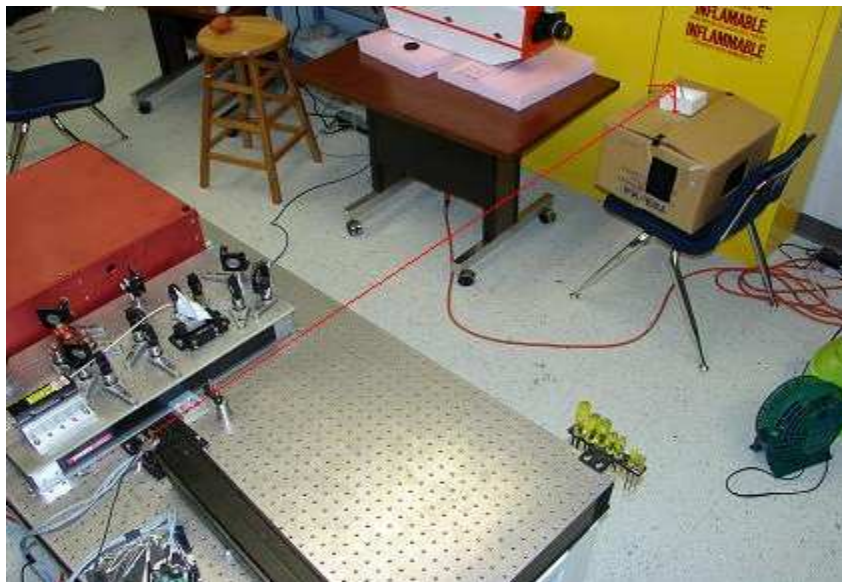


Figure 4.2 Photograph showing the incense sticks, DRS Hadland camera and the direction of laser propagation.



Figure 4.3 Photograph showing the incense sticks which created the flow field fixed in thermocole

The camera used for imaging was DRS Hadland Ultra68. It has been described in Section 3.4 . The camera was operated at 1000 frames/sec, its slowest framing rate. The camera captured 68 images in each image sequence with the exposure time of each image being 1 millisecond (ms) thus, the overall exposure time being 68 ms. The resolution of each image was 220\*220 pixels. The motion of the mirror was controlled by a staircase waveform where each step of the staircase corresponded to a particular location of the mirror. The camera was triggered such that the exposure time of each image corresponded to a given location of the mirror exactly in time. This was done to maximize the signal that could be accumulated for every image in the image sequence. The synchronization was achieved using Labview 8.0 code and a NI6251 DAQ board which created the staircase waveform.

The code of the program served a dual purpose of creating a staircase waveform for controlling the scanning mirror and creating a trigger for the camera operation. Figure

4.4 shows the code of the program. The inner loop of the code creates one cycle of the waveform. Each cycle of the waveform consists of a finite number of steps where each step has a finite amplitude. For the current experiments this finite amplitude equals 0.006 Volts, which is input to the scanning mirror and corresponds to an angular step of xxx degrees. The amplitude of each step corresponds to the distance the mirror rotates before reaching the next scan position. The total voltage supplied to the mirror was 68 times 0.006 volts equaling 0.408 volts and the total sweep of the mirror was 2.652 degrees. Each step of the waveform was 1ms long which meant that the mirror waited for 1ms at a given scan location before moving on to the next scanning position. The offset value is used to shift the entire staircase waveform relative to zero. The outer loop of the code duplicates a single cycle by the desired number of cycles.

Figure 4.5 shows the code for generating the trigger for camera operation in simultaneity with the staircase waveform. The camera was triggered such that 1 millisecond exposure of the camera exactly overlapped with the 1 millisecond the mirror waited at a particular scan position. In order to do a trigger signal was generated from labview which was almost coincident with the edge of the staircase waveform. This signal was fed into a signal generator where it was fine tuned to exactly match the edge of the staircase. The advantage of using labview is that it allows for the use of different clocks to create triggers with varying time resolution. In the current case we used a 100 kHz time base to create a trigger signal with millisecond resolution. Figure 4.6a shows the staircase waveform and figure 4.6b shows the enlarged view of the staircase waveform with the steps clearly visible and figure 4.6c shows the input parameters for the labview code.

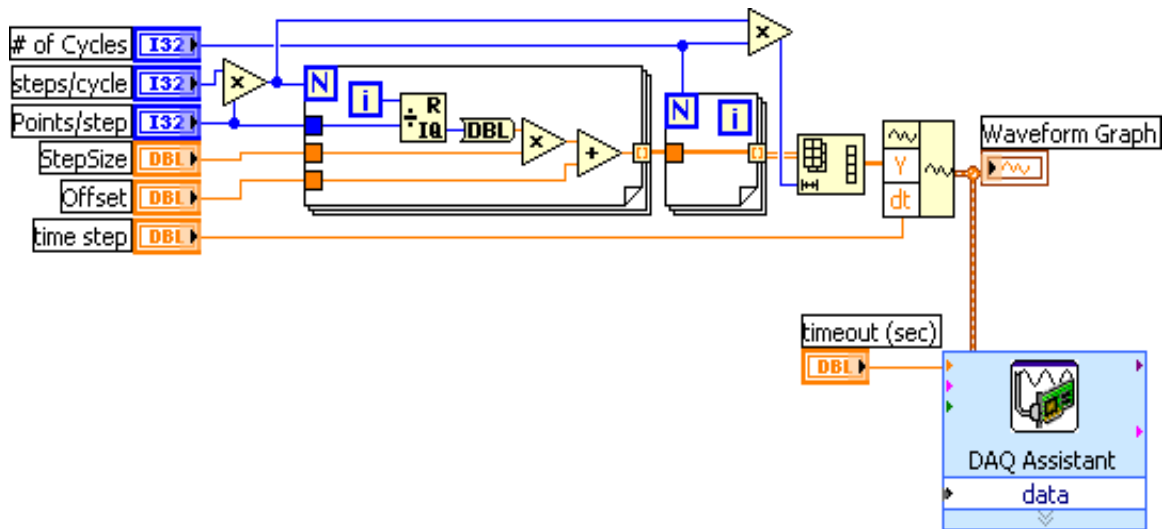


Figure 4.4 Labview block diagram for generating the staircase waveform.

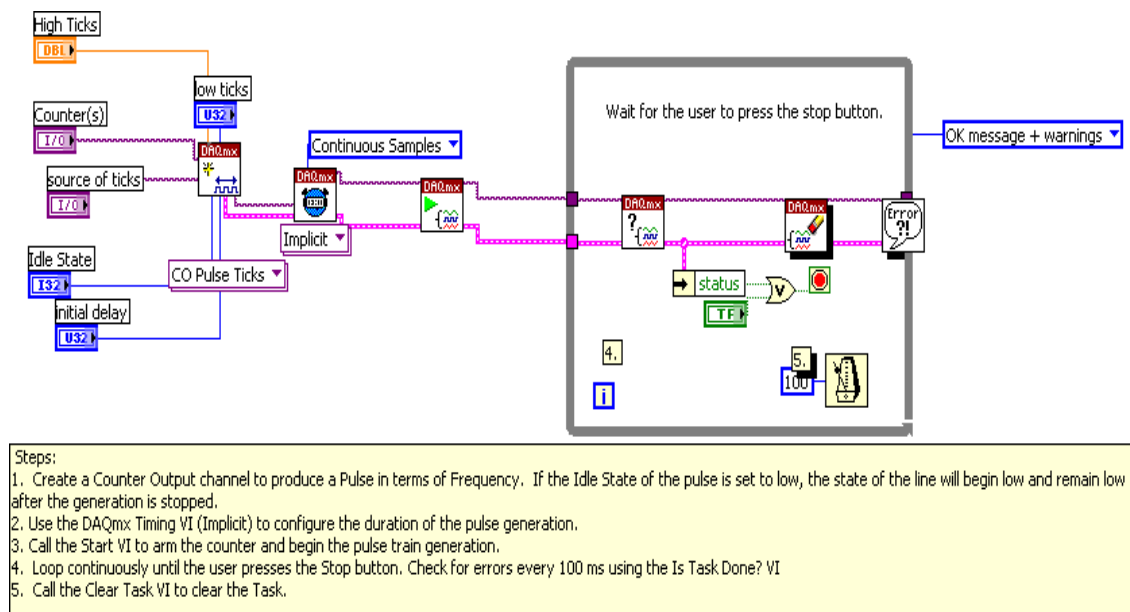


Figure 4.5 Labview block diagram for creating a trigger signal for triggering the camera.

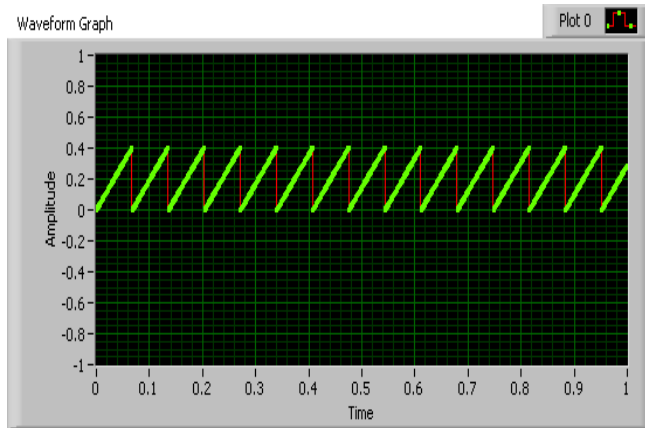


Figure 4.6a Staircase waveform generated to control the mirror location



Figure 4.6b Enlarged view of the staircase waveform between 0 to 0.14V. The steps in the staircase are clearly visible.

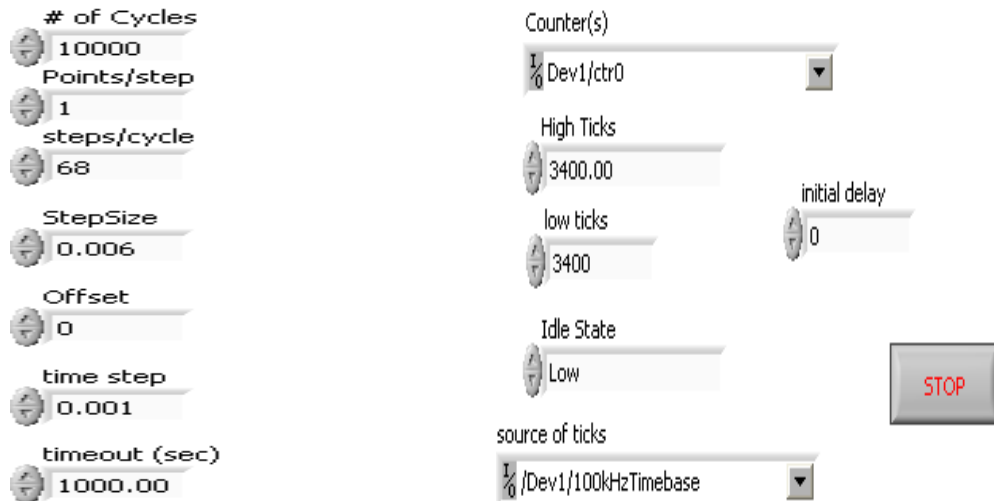


Figure 4.6c The input parameters for the staircase waveform are given above. The numbers above indicate the input parameters for the trigger waveform above.

We found that Labview provided us with the flexibility of generating various type of waveforms in terms of amplitude, frequency and shape of the waveform. This in turn leads to custom control of the mirror movement and the ability to simultaneously trigger the camera. We believe that given the operating range of labview it would be instrumental in synchronizing equipment in any modern laboratory.

### 4.3 Experimental results

The 68 images, each of which corresponded to a different 2-D slice of the flow field, were transferred to a computer for post-processing in Matlab. The images first underwent dot card correction. Dot card correction may be used in different ways depending on the application. In the current application it was used to remove the image to image jitter. The jitter occurs since the images are being recorded on to four different quadrants of the CCD in a cyclic manner and due to slight difference in the alignment of the image on to a CCD quadrant the image of the same object tends to shift between images. A dot card is

essentially a matrix of black dots on a white background. Figure 4.7 is a photograph of the dot card.

The dot card is at least as large as the target field of view. The correction process involves first taking sample images of the dot card then one of these images is chosen as the reference image. The other images of the dot card are then corrected to be as similar as possible to the reference image. This is a manual process and involves the realigning of dots in one dot card image to match the position of dots in the reference image. Since the camera uses four quadrants from a single CCD, only the 1<sup>st</sup> 3 images were required to be aligned to the 4<sup>th</sup> one. The other 64 images can be automatically aligned by using the transformation information obtained from the manual alignment process. The next correction done was low-pass filtering; this is done in order to remove noise in the camera occurring due to random statistical fluctuations of incident photons on the CCD surface.

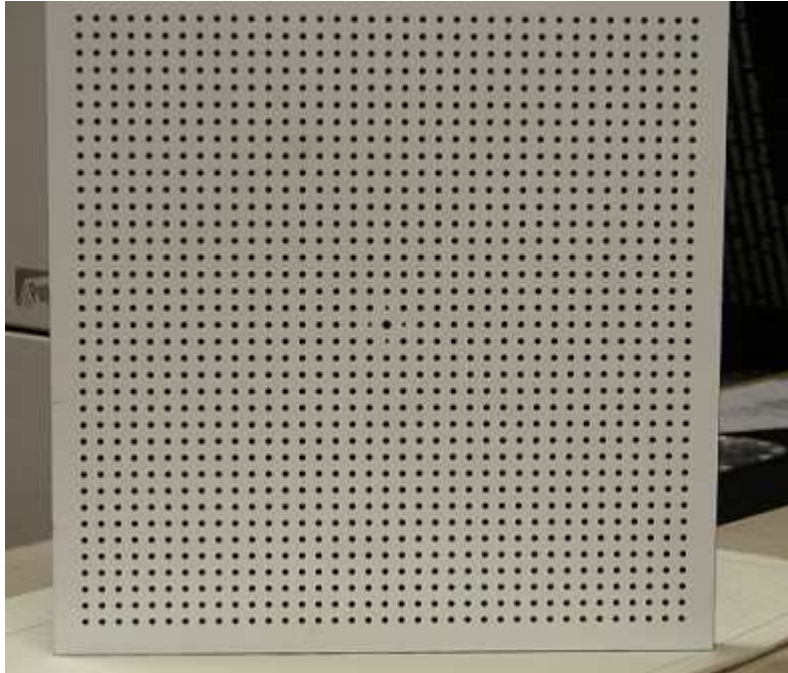


Figure 4.7 - Photograph of a dot card used for image registration.

The flow from the incense sticks initially starts out laminar. Figure 4.8 shows a sequence of 12 images (out of 68) of the laser sheet passing through the incense smoke. The individual laminar plumes rising out of the four different incense sticks are distinctly visible. It is important to note that each image corresponds to a different 2-D slice of the flow field. The first few images show the plumes from the incense sticks located closest to the camera and the last few frames show the smoke plumes furthest away from the camera.

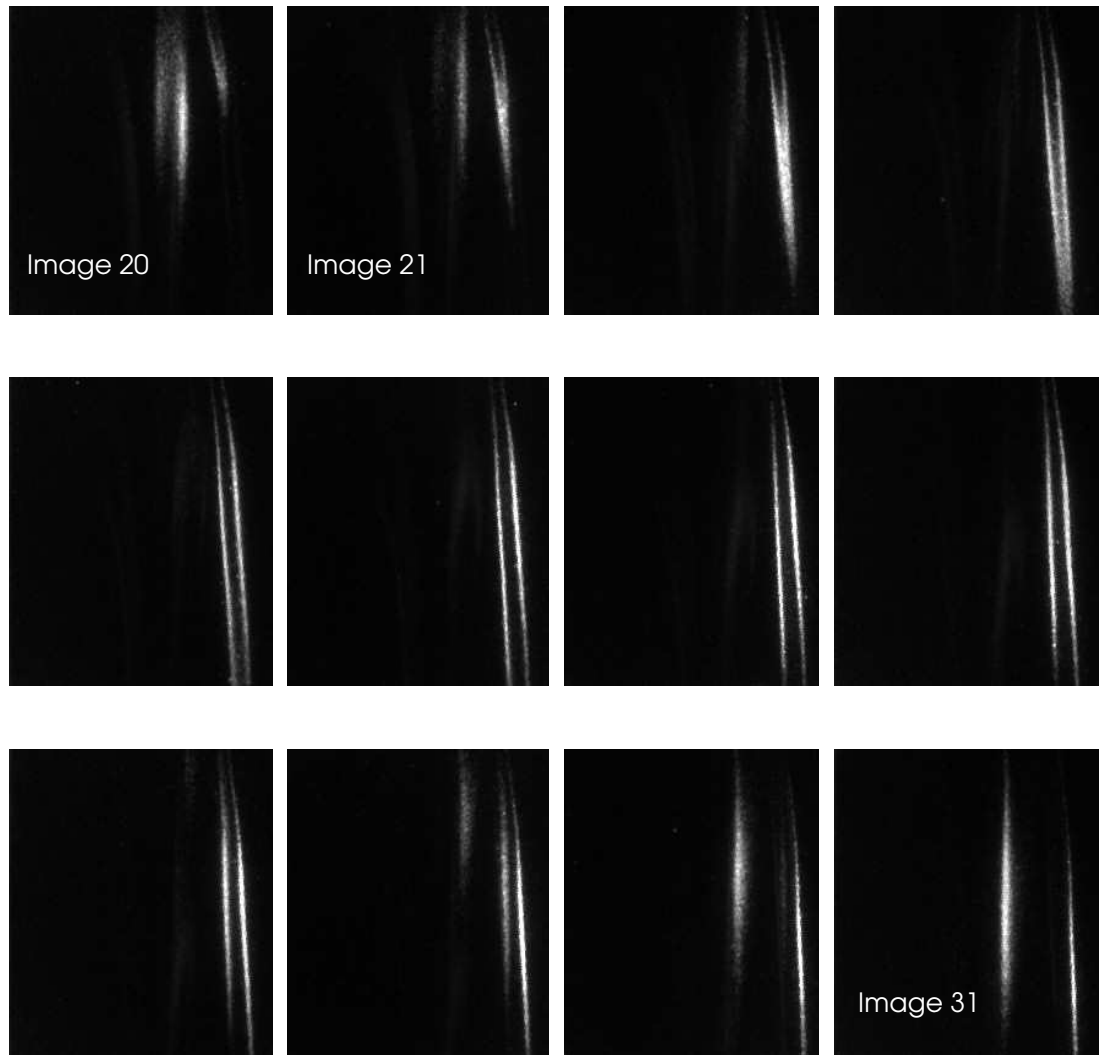


Figure 4.8 Twelve images (out of a 68 image sequence) of the scattering of light from rising smoke. Each frame constitutes a different 2-D slice through the flow field.

The true strength of the imaging technique is, of course, the ability to produce 3-D images. Figure 4.9a and 4.9b show two different views of a reconstructed 3-D image made from the same sequence of images used to produce Figure 4.8. The images were reconstructed in Matlab using, among others, the function `isosurface`. This function takes three-dimensional scalar data and computes a surface corresponding to a constant value within the 3-D data field. In this case, the value was image intensity with a numerical

value of 25 (out of 255) chosen to produce the images in Figure 4.9. This threshold was above the background noise threshold of the images, but low enough to capture most of the observable flow structure. The contrast between the smoke and the surrounding air was distinct enough that the choice of intensity threshold does not greatly affect the 3-D images presented here. It is estimated that the use of pulse burst laser would improve the signal by 500 times even with a conservative estimate of 5mJ/pulse for a 20ns pulse. The increase in pulse energy would allow the experimenters to reduce the overall exposure time 500 times to 134  $\mu$ sec and still obtain a signal as good as the one obtained in these experiments. This reduced exposure time is necessary to obtain nearly-instantaneous images of high-speed flows.

The amount of information contained in Figure 4.9 is substantial and clearly easier to interpret than the sequence shown in Figure 4.8. In this case, the flow appears to be laminar and the number of smoke plumes (4) is clear. The reference axis is indexed by the pixel count and the scan direction of the laser is indicated. Even in this laminar case, there are interesting features that would be difficult to identify without use of a 3-D imaging technique. For example, the crescent cross-sectional shape of the smoke plume at the back of the image (uppermost plume in 4.9b) would be difficult to visualize and might be assumed to be round in cross-section based on lesser information. This particular feature is attributed to the smoke rising up and around the incense stick.

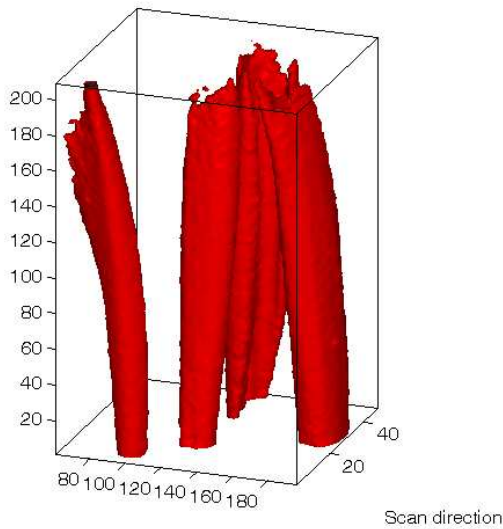


Figure 4.9a 3-D picture of smoke rising from four incense sticks. Image is taken within the laminar regime of the flow.

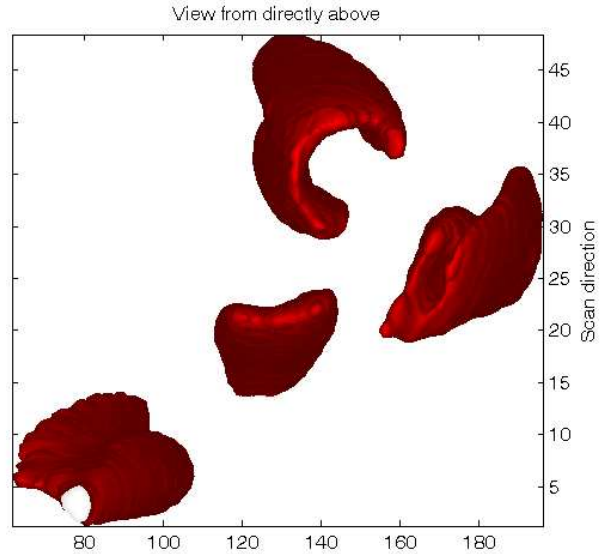


Figure 4.9b Overhead view of Fig. 4.9a showing more detail about the 3-D structure of the smoke plumes.

The tremendous potential of the technique for 3-D flow visualization becomes even clearer when the flow is disturbed by shaking the base holding the incense sticks. This causes the flow to transition from the laminar to the turbulent flow regime and leads to interaction between the four smoke plumes. Figure 4.10 shows 12 2-D images of flow in transition from laminar to turbulent. Please note that the flow velocity is small enough that the flow is nearly stationary within a time interval of 68 ms. The perceived motion in the images below is due to the laser sheet scanning across the flow field. One can see how a mushroom vortex slowly comes into view with its best visibility in image 28 and then as the sheet progresses on the mushroom vortex goes out of the illuminated area.

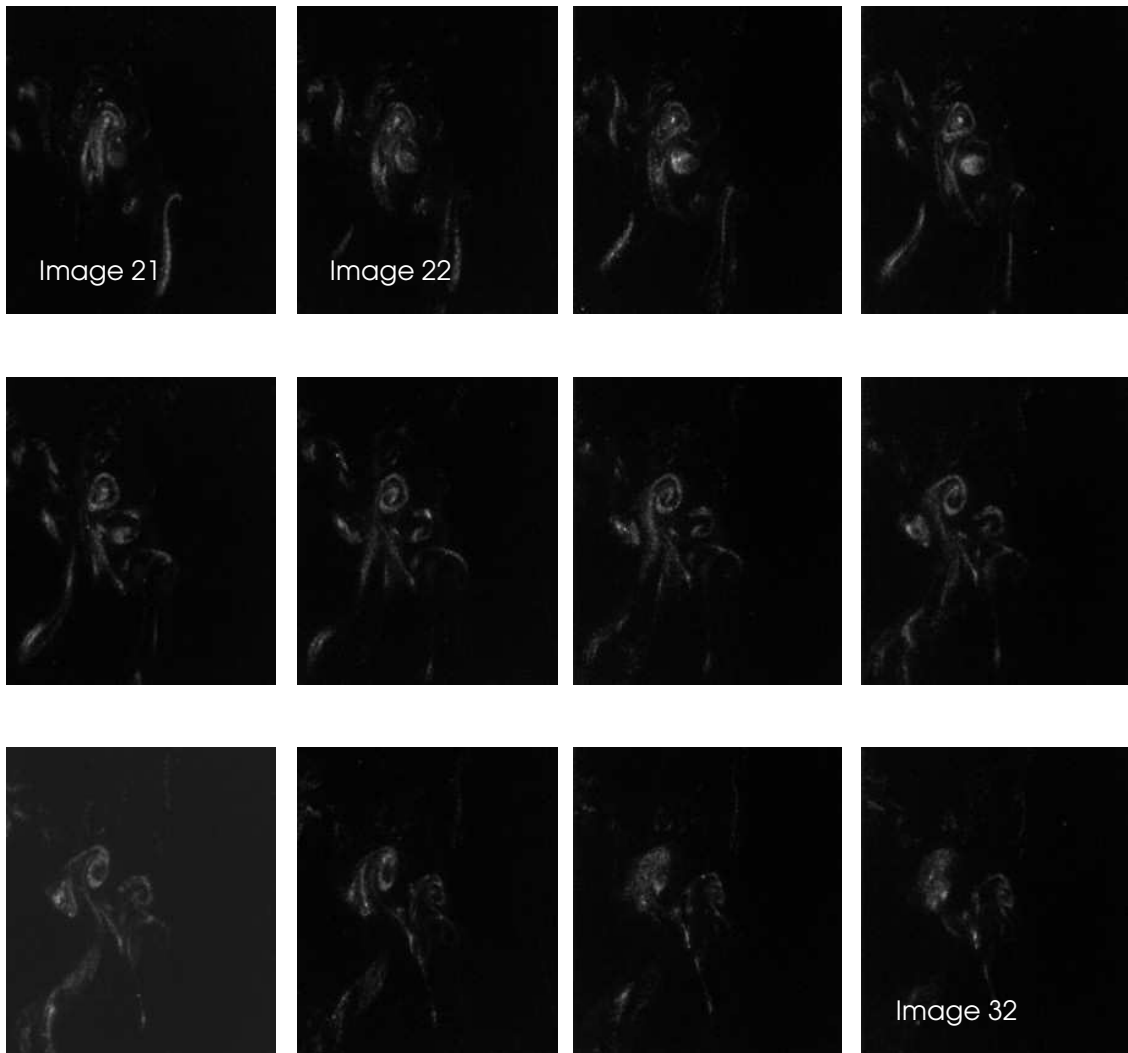


Figure 4.10 Twelve images (out of a 68 image sequence) of the scattering of light from rising smoke. Each frame constitutes a different 2-D slice through the flow field.

The above set of images also underwent 3-D reconstruction. Figure 4.11a is the 3-D reconstruction of the entire flow field. Of note is a large-scale vortical structure near the front of the image. It is also possible to zoom in on a particular feature. Figure 4.11b is the enlarged view of the large vortical structure.

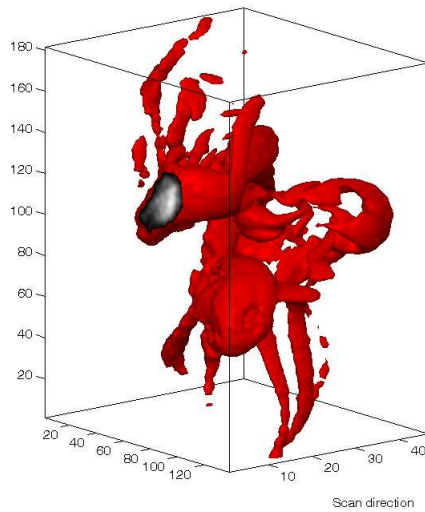


Figure 4.11a 3-D image of smoke subjected to a disturbance forcing transition.

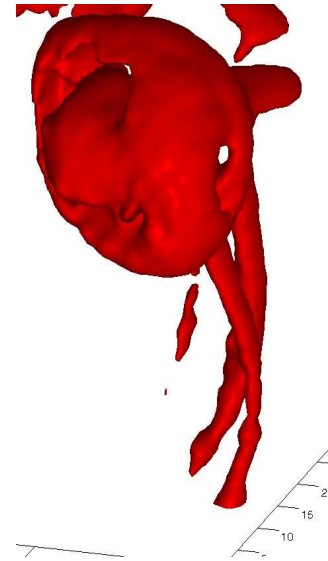


Figure 4.11b Enlarged view of the flow structure towards the front in 4.10a.

The other interesting feature of Matlab image processing is its ability to show cross-sectional views of the flow field. Figure 4.12a shows the cross-sectional view of a section passing through the large flow structure towards the front. The cross-sectional view reveals a pair of counter-rotating vortices. An enlarged view of the mushroom vortex is shown in figure 4.12b. The mushroom vortex is characterized by counter rotating vorticity. The same vortex could be seen in the sequential 2-D images in figure 4.10 above.

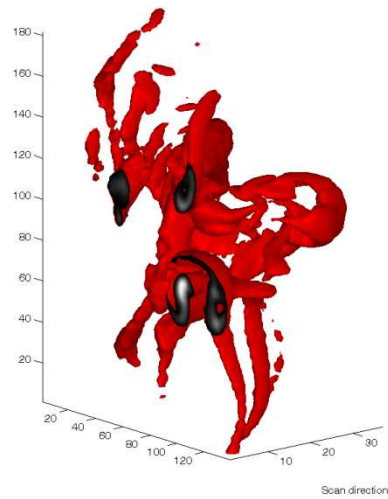


Figure 4.12a Cross-Sectional view of the front facing flow structure in 4.11 a



Figure 4.12b Enlarged view of the counter rotating vortices in 4.11 a.

As the flow progressed from laminar to turbulent the interactions between the plumes increased. This interaction is visible in the form of smooth intertwining between the plumes in figure 4.13a. It seems that the individual plumes have bifurcated and multiplied in number with each of these new divisions branching out and entangling with each other. Further progression towards turbulence leads to a complete breakdown in the flow. The flow is now all mixed up and it is hard to discern any separate flow structures. This turbulent breakdown of flow is shown in figure 4.13b.

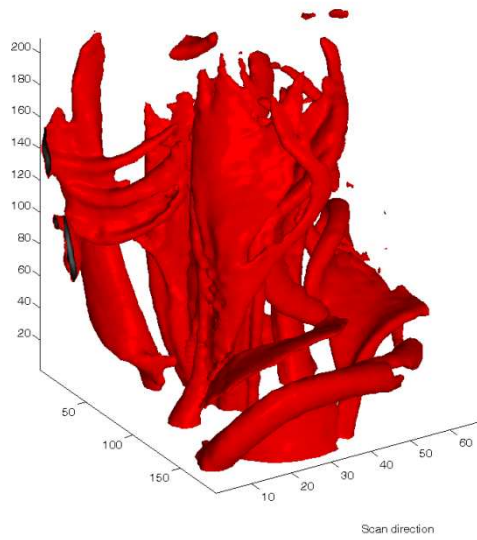


Figure 4.13a 3-D image of interacting smoke plumes as they transition to turbulent flow.

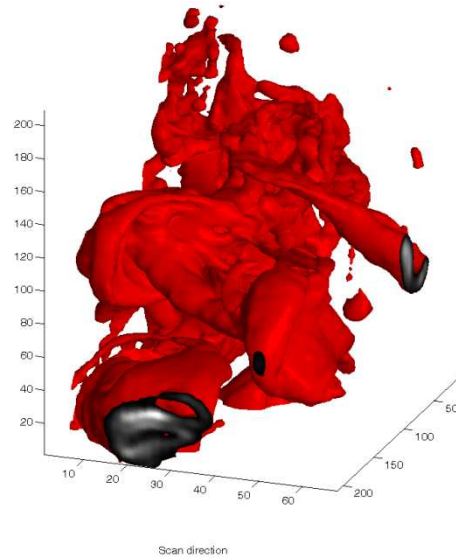


Figure 4.13b 3-D image of interacting smoke plumes in turbulent regime.

Several more images including those of different flow fields were obtained during low speed 3-D flow visualization experiments. Only some of them have been presented in this work. The interpretation of qualitative information in flow imaging is always subject to the experience of the observer. The reader is encouraged to take a close look at these figures to appreciate the wealth of information they contain. It is also interesting to note that what we call “low-speed” may, in fact, be fast enough for many other applications. All that was needed for the current experiments was a HeNe laser, a scanning mirror and a high-speed camera. The laser and camera are components that may be readily available in other laboratories and the scanning mirror can be acquired relatively inexpensively (~\$2k). Thus, the present results illustrate that many laboratories may have the capacity to perform 3-D flow visualization with already existing equipment. One potentially interesting application would be to couple the current technique with a high-speed CMOS camera (e.g. Vision Research, Photron or Red Lake), which is capable of sustaining

frame rates of 1,000 fps over several thousand images. This would enable time-resolved 3-D flow-visualization where 3-D flow visualization movies could be produced.

## 5 CONCLUDING REMARKS

A three-dimensional laser scanning technique has been developed at the Advanced Laser Diagnostics Laboratory (ALDL) at Auburn University. The 3-D images obtained using this technique has been presented in chapter 4. Even though the images obtained were of a low speed flow using a 15mW HeNe laser, they clearly demonstrate the efficacy of the mirror and camera and demonstrate the overall concept of 3-D imaging using laser scanning. Unfortunately due to a problem in the electrical power supply the pulse burst laser could not be completely characterized and used for the described experiments. The 3<sup>rd</sup> generation pulse burst laser provides flexibility in terms of pulse repetition rate and pulse duration and therefore can be used as a light source for varied applications. Future work would include measuring the maximum gain of the system with all the amplifiers in operation. Further characterization would include measuring the uniformity in the energies of multiple pulses at different repetition rates. The optimization of the location of the burst of pulses would be an iterative but would lead to more uniformity amongst the pulses at a greater average energy. The inclusion of the 3<sup>rd</sup> generation pulse burst laser would allow 3-D imaging of a range of flows ranging from slow natural convection driven slow flows to high-speed reacting, mixing flows in a supersonic combustion ramjet (SCRAM). The pulse burst system which currently provides a gain of approximately  $10^7$  maybe scaled up to include 1-2 more amplifiers and thus provide a cumulative gain of  $10^9$ . This would not only allow the use of the pulse burst laser to scan larger volumes but also its application more beneficial in harsher environments such as reacting flows which cause attenuation of the laser beam.

It would also allow the extension of other techniques like Rayleigh scattering to three dimensions where the signal is weaker than Mie scattering.

The scanning of the laser has been accomplished using a galvanometric scanning mirror. The mirror is controlled through a Labview code. Labview allows the creation of customized waveforms which means that the mirror can be operated at any speed desired. Thus, one would need to invest in only one galvanometric scanning mirror to obtain 3-D images for flows with varying velocities.

The reconstruction of 3-D images has motivated researchers at ALDL to explore other image post processing tools. Although MATLAB was used for the experiments conducted other software packages such as Tecplot offer manipulation of intensity data. We anticipate that the exploration of other image post-processing options would lead to better insights into flow structure. Other issues pertaining to 3-D imaging such as optimization of depth-of-field vis-à-vis the intensity of the signal obtained and the effect of changing magnification during laser scanning on the quality of images are being investigated. An enhanced understanding of 3-D imaging would be crucial to the production of high quality images.

Although the present work discusses the development of a qualitative technique it is conceivable to extend this technique to be quantitative. Techniques like particle image velocimetry (PIV) and planar laser induced fluorescence (PLIF) which are widely implemented in 2 dimensions maybe extended to 3 dimensions. 3-D PLIF would involve 3-D reconstruction of the flow field from a series of 2-D images, each of which would be related to the flow field variables by a mathematical model. However, we anticipate a

more complicated calibration process since it would be necessary to account for pulse to pulse fluctuations and the change in intensity of a 2-D image with varying distance from the camera in addition to the standard 2-D calibration. In order to implement 3-D PIV a set of pair of correlated images would be required. These may be obtained by using 2 galvanometric scanning mirrors along with an acousto-optic deflector (AOD). The AOD could be used to deflect the laser pulses towards one mirror and upon completion of a scan in one direction, can be used to deflect the laser pulses towards the second mirror which would then scan the laser in the opposite direction. By careful alignment of the involved devices high-speed 3-D PIV can be achieved. The other important consideration for obtaining quantitative results is that the signal to noise (SNR) ratio of the imaging camera should be high. The DRS Hadland Ultra 68 camera which is being currently used at ALDL is an intensified charge coupled device and due to its inherent design has a low SNR. Thus, that camera was not used to obtain quantitative results.

To summarize the work done towards the development of 3-D flow visualization technique is an ongoing endeavor which already promises exciting possibilities. The development of its components like the pulse burst laser in itself offers varied applications. The potential extension of qualitative high speed 3-D imaging to a 3-D quantitative measurement tool would have far reaching consequences in the field of experimental fluid dynamics.

## REFERENCES

- Buch Jr, K.A. and Dahm, W.J.A. , “Experimental study of the fine-scale structure of conserved scalar mixing in turbulent shear flows,” *Journal of fluid mechanics*, pp1-29, 1998.
- Clemens, N.T., “Flow Imaging,” *Encyclopedia of Imaging Science and Technology*, John Wiley and Sons, New York, 2002.
- Elkins, C.J., Markl, M., Pelc., N. and Eaton, J.K., “4D Magnetic resonance velocimetry for mean velocity measurements in complex turbulent flows,” *Exp. Fluids*, Vol. 34, pp. 494-503, 2003.
- Goldstein, J.E. and Smits, A. J., “Flow Visualization of the Three-Dimensional, Time-Evolving Structure of a Turbulent Boundary Layer,” *Phys. Fluids*, Vol. 6, pp. 577-587, 1994.
- Grace, J.M. , Nebolsine, P.E. and Goldey, C.L., “Repetitively pulsed ruby lasers as light sources for high-speed photography,” *Opt.Eng.*37, 2205-2212 (1998).
- Guezennec, Y.G., Brodkey, R.S., Trigui, J. and Kent, J.C. “Algorithms for fully automated three-dimensional particle tracking velocimetry,” *Exp. in Fluids*, Vol. 17, pp. 209-219, 1994.

- Huntley, J.M., "High-speed laser speckle photography. Repetitively Q-switched ruby laser light source," *Opt. Eng.* 33,1692-1699 (1994)
- Hult, J., G.Josesson, M.Alden and C.F. Kaminski, "Flame front tracking and simultaneous flow field visualization in turbulent combustion", presented at the 10th International symposium on applications of laser techniques to fluid mechanics, Lisbon, Portugal, 10-13 July 2000.
- Island, T.C., Patrie, B.J., Mungal, M.G. and Hanson, R.K., "Instantaneous Three-Dimensional Flow Visualization of a Supersonic Mixing Layer," *Exp. Fluids*, Vol. 20, pp. 249-256, 1996.
- Kastengren, A., Dutton, J. and Elliott, G., "Time-Correlated Visualizations of Supersonic Blunt-Base Cylinder Wakes," AIAA Paper 2005-1346, 43rd AIAA Aerospace Sciences Meeting and Exhibit, Reno, Nevada, Jan. 10-13, 2005
- Korpel,A, "Acousto-Optics", Second Edition, 1997
- Laufer,G, "Introduction to Optics and Lasers in Engineering", Second Edition, 1996
- Lempert, W. R., Wu., P., Zhang, B., Miles, R. B., Lowrance, J. L., Mastracola, V., and Kosonocky, W. F., "Pulse-burst laser system for high speed flow diagnostics," AIAA Paper 96-0179, (1996).
- Patrie, B.J., Seitzman, J.M., and Hanson, R.K., "Instantaneous Three-Dimensional Flow Visualization by Rapid Acquisition of Multiple Planar Flow Images," *Opt. Eng.*, vol. 33, pp. 975-980, 1994.

- P. Wu, W. R. Lempert, and R. B. Miles, "MHz pulse-burst laser system and visualization of shock-wave/boundary-layer interaction in a Mach 2.5 wind tunnel," *AIAA J.* 38, 672-679 (2000).
- Royer, H., "Holography and particle image velocimetry," *Meas. Sci. Technol.*, Vol. 8, pp. 1562-1572, 1997.
- Smits, A.J., and Lim.T.T., "Flow visualization: Techniques and Examples," Imperial College Press, London, 2000.
- Su, L.K. and Clemens, N.T., "Planar measurements of the full three-dimensional scalar dissipation rate in gas-phase turbulent flows," *Exp. Fluids*, Vol. 27, pp. 507-521, 1999.
- Thurow. B., Jiang. N., Samimy.M., and Lempert.W., "Narrow-Linewidth Megahertz-Rate Pulse-Burst Laser for High-Speed Flow Diagnostics," *Applied Optics*, Vol. 43, No. 26, pp. 5064-5073 (2004).
- Thurow, B., Jiang, N., Lempert, W. and Samimy, M., "MHz Rate Planar Doppler Velocimetry in Supersonic Jets," *AIAA Journal*, Vol. 43, No. 3, pp. 500-511, March 2005.
- Thurow, B. and Satija, A., "Design of a MHz Repetition Rate Pulse Burst Laser System at Auburn University," *AIAA Paper 2006-1384*, 44th AIAA Aerospace Sciences Meeting and Exhibit, Reno, NV, 2006
- Thurow, B. and Satija, A., "Preliminary Development of a Nearly-Instantaneous Three-Dimensional Imaging Technique for High-Speed Flow Fields," *AIAA Paper 2006-*

2972, 25th Aerodynamic Measurement Technology and Ground Testing Conference, San Francisco, CA, June 2006.

Thurow, B. and Satija, A., "Further Development of a High-Speed Three Dimensional Flow Visualization System," AIAA Paper 2007-1060, 45th AIAA Aerospace Sciences Meeting and Exhibit, Reno, NV, 2006

Wernet, M., and Opalski, A., "Development and application of a MHz-frame rate PIV system," AIAA Paper 2004-2184, 2004.

Wu, P. and Miles. R.B., "High-energy pulse-burst laser system for megahertz-rate flow visualization", Optics Letters, Vol. 25, No. 22, pp 1639-1641, 2000.

Yip, B., Schmitt, R.L., and Long, M.B., "Instantaneous, Three-Dimensional Concentration Measurements in Turbulent Jets and Flames," Opt. Letters, Vol. 13, pp. 96-98, 1988.